# INTEGRATING RELIABILITY INTO PERFORMANCE-ORIENTED DESIGN OF FAULT-TOLERANT SWITCH-MODE DC-DC CONVERTERS FOR PHOTOVOLTAIC ENERGY-CONVERSION APPLICATIONS

BY

SAIRAJ VIJAYKUMAR DHOPLE

THESIS

Submitted in partial fulfillment of the requirements
for the degree of Master of Science in Electrical and Computer Engineering
in the Graduate College of the
University of Illinois at Urbana-Champaign, 2009

Urbana, Illinois

Adviser:

Professor Patrick L. Chapman

## ABSTRACT

This work bridges the disconnect between two consequential design concerns in switch-mode power converters deployed in photovoltaic energy-processing applications: steady-state performance, evaluated through metrics such as ripple in pertinent voltages and currents, and reliability, evaluated through metrics such as mean time to system failure.

Paying due regard to the growing adoption of topologically redundant power converters, a general framework for fault-tolerant design is presented in the context of a multiphase, interleaved boost converter. A unified, system-level, steady-state description for this topology is proposed. The analyzed model includes conduction losses in the coupled inductor and switches. An interleaved switching scheme governed by ripple correlation control tracks the maximum power point of the photovoltaic source. The theoretical derivations are validated against detailed numerical simulations, and their applicability over a wide range of ambient conditions is demonstrated.

The steady-state characterization of the converter is then employed to specify the failure rates of circuit components and establish the effects of ambient temperature, insolation, number of phases, and device ratings on system reliability. Acknowledging the dependence of the failure rates on operational conditions, a Markov reliability model is derived to assess the reliability of a general *N*-phase converter. The proposed analytical tools provide a methodical framework for design of fault-tolerant, multiphase converters employed in a wide range of photovoltaic systems.

To *Papa* and *Ayee*

## ACKNOWLEDGMENTS

First and foremost, I owe a debt of gratitude to my adviser, Professor Patrick Chapman, for the opportunity he has given me to study and perform research at the University of Illinois at Urbana-Champaign. In addition, I am grateful to him for providing me the opportunity to lead the electrical engineering team of the University of Illinois at the 2009 Department of Energy's Solar Decathlon. I wish to extend a warm thanks to him for all his support, guidance and advice.

I have thoroughly enjoyed my course work in power electronics and electric machines taught by Professor Philip T. Krein, and I wish to thank him for having sparked my interest in these areas.

Professor Jonathan Kimball inducted me into the power-electronics research group while he was a research engineer at the Grainger Center for Electric Machines and Electromechanics. Working under his guidance was an incredible learning experience. In addition, I would like to extend a warm welcome to Professor Alejandro Domínguez-García. Our discussions ultimately developed into the chapters on reliability in this thesis, and his out-of-the-box thinking has shaped many of the concepts outlined henceforth. I wish them both great successes in their forthcoming academic endeavors.

I cannot express my gratitude in words for the unflinching support and unconditional love that my family and friends have provided over the years I have spent away from home.

## TABLE OF CONTENTS

# CHAPTER 1

# INTRODUCTION

Multiphase, switch-mode converters have been adopted widely in voltage regulator modules [1], power factor correction circuits [2], hybrid electric vehicles [3], distributed power supplies [4] and recently, photovoltaic (PV) systems [5]-[8]. Compared to conventional switch-mode power converters, multiphase converters can be designed to enjoy lower current and voltage ripple, improved dynamic performance with lower values of filter components, and they offer improved reliability given the inherent topological redundancy. However, these converter topologies present unique design challenges with respect to switching techniques and magnetic design. Some of the control-related concerns are addressed in [9], which introduces a distributed control approach for multiphase topologies. The scheme requires no central control, can account for a varying number of converters and is highly reliable. Magnetic design considerations for general multiphase, dc-dc converters are explored in [10]-[11].

Multiphase boost converters with interleaved switching have received considerable interest in PV applications. For instance, reference [12] introduces a coherent state-space averaging method to analyze a two-phase interleaved boost converter with coupled inductors. The authors emphasize the benefits of the proposed topology by comparing coupled and non-coupled interleaved boost converters for PV applications. A hardware prototype of a three-phase, interleaved boost converter for a PV source is demonstrated in [13]. The proposed circuit topology employs a maximum power point tracking (MPPT) algorithm based on the extremum-seeking principle [14] and introduces an additional control loop for current balancing.

Conventional multiphase, boost converters with DC inputs are well documented and analyzed. Generalized steady-state analysis of a multiphase, interleaved boost converter using coupled inductors and corresponding small-signal models are presented in [15] and [16], respectively. The benefits of strongly coupled inductors in interleaved boost converters are further expounded in [17], where it is demonstrated that the topology enjoys superior current-sharing characteristics and small input current ripple. However, PV applications present unique modeling challenges. Traditional state-space averaging techniques fail to capture the non-linear, time-varying character of the PV source. Consequently, it appears that design choices for analogous converters have hitherto not relied on accurate analytical models; rather, they have

been based on expected behavioral norms of such systems. The models developed in this work present the circuit designer with a potent set of tools to not only aid in the design of multiphase converters, but also set forth a framework for reliability assessment and fault-tolerant design.

Reliability of PV energy conversion systems is of paramount concern owing to the high fixed costs of such installations and also due to the mission-critical nature of certain applications, e.g., satellites. Traditionally, research in this area has focused on the reliability of PV modules [18]-[19], and unfortunately, the circuits dedicated to PV sources have not been the subject of rigorous scrutiny. Notwithstanding this fact, practical considerations from the perspective of balance-of-system components are well detailed in [20], and in [21] a systematic approach to studying the reliability of power-electronic circuits in PV systems is established and demonstrated with a real-world example. Congruently, with the growing adoption of grid-tied PV applications, there has recently been increased attention paid to the reliability of grid-tied inverters [22]. A circuit topology similar to that considered in this work is analyzed with a reliability-oriented perspective in [23]. It is demonstrated that employing derated semiconductor devices enables the construction of more reliable converters without resorting to soft-switching techniques. References [24]-[25] examine the reliability of different circuit topologies applied to PV applications with the objective of identifying the weakest link in the design. The results indicate that the switching stage is most likely to fail and temperature is revealed as the most likely cause of failure.

Circuit topologies aside, a multitude of other aspects potentially dominate reliability of PV energy systems. An exhaustive overview of such concerns is well documented in [26]. General topological concerns of the nature highlighted thus far are presented and it is concluded that the PV modules themselves are among the most reliable components of a typical system. Apprehensions related to energy storage (batteries), energy-processing equipment (dc-dc converters) and balance of system components are adequately addressed based on an extensive literature review. More motivating are perhaps the emerging concerns associated with the reliability of anti-islanding techniques and MPPT algorithms, as these areas have not been analyzed satisfactorily thus far.

Research in reliability assessment of fault-tolerant, switch-mode converters has been severely limited and one-dimensional. Primarily, the main ambient condition that features into conventional reliability studies is temperature. The effects of insolation are assumed to have no bearing on the stress imposed on power-electronic circuits. This is a glaring omission as the

power output of PV arrays is directly related to the amount of insolation received. The power processed—and indeed the losses, reverse voltages and heat dissipation—are to a large extent governed by incident insolation. Factoring this effect into the analysis is complicated, primarily owing to the non-linear nature of the PV source and a lack of suitable models for multiphase converters. Second, incident insolation and ambient temperature are both functions of the time of the day and season of the year. This presents unique challenges to estimating the reliability of a PV installation over an extended period of time (say over the lifetime of the module), and meaningful assumptions need to be formulated for accurate assessment. Third, it has been observed that empirically accepted, system-level traits generally guide design choices. For instance, structural redundancy is expected to translate to improved reliability and aluminum electrolytic capacitors are largely disregarded as unreliable. While these statements are contextually true, for the reasons highlighted earlier, academically interesting yet practically perplexing trade-offs emerge in PV installations. Finally, there is a subtle trade-off between converter performance and system reliability. In [27], a coherent methodology for integrating reliability considerations into the analysis carried out for the design of fault-tolerant power converters is presented. A design approach is offered wherein, for any uncontrolled input, the state variables remain within a region of the state space defined by performance requirements. Unfortunately, the non-linearity of the source makes it mathematically intractable to employ similar tools for analysis.

The analytical description of the converter is indispensable to quantifying overall system reliability. Factors such as voltage ripple dealt with by filter capacitors and losses in the active switching devices and diodes determine the failure rates of these devices. Ambient temperature and solar insolation determine the terminal voltage and current sourced by the PV module, and in turn affect the stresses on the components in the converter. A meaningful reliability assessment demands an accurate steady-state description and both aspects are given equal attention in the forthcoming analysis.

Chapter 2 introduces the models that describe the fault-tolerant converter, PV module, MPPT controller, coupled inductor and metrics commonly utilized to gauge the performance of PV energy-conversion systems. The steady-state operation of an $N$-phase, interleaved converter is examined in detail in Chapter 3. Closed-form expressions are derived to evaluate consequential metrics such as the output voltage, output voltage ripple, input current ripple, duty ratios of switching devices and converter efficiency. The validity of the theoretical models is affirmed by

comparison with detailed switched simulations. Fidelity over a wide range of operational conditions (ambient temperature, incident insolation) is demonstrated. Chapter 4 sets forth the framework that is utilized to evaluate the system reliability. Failure-rate models are highlighted for the different components in the converter, and their variation with ambient conditions and converter design is probed. Finally, Chapter 5 describes the Markov reliability models used to assess the reliability of a general *N*-phase converter. Novel metrics that acknowledge system performance and reliability are introduced and evaluated for two- and three-phase converters. Case studies are drafted to quantify the impact of design parameters such as switching frequency and voltage rating of components on system reliability. Insights gained through the case studies are utilized to formulate a general strategy for fault-tolerant design in PV energy-conversion systems.

# CHAPTER 2

# RELEVANT MODELS

This chapter describes the models of the multiphase boost converter, coupled inductor, PV module and MPPT controller employed in this work. Metrics to quantify the performance of PV energy-conversion systems are also introduced.

## 2.1 Multiphase, Interleaved Boost Converter Model

A multiphase converter transfers power between a single input and a single output through redundant phases. The definition is illustrated in Figure 1, which also depicts a multiple-input, single-output converter for comparison. Figure 2 depicts a three-phase example of the general class of multiphase converters considered in this work.

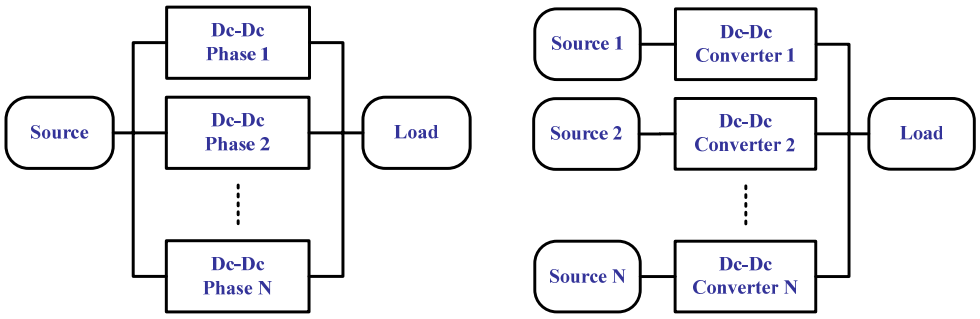


Multiphase converter Multiple-input converter

**Figure 1:** Multiphase and multiple-input dc-dc converters

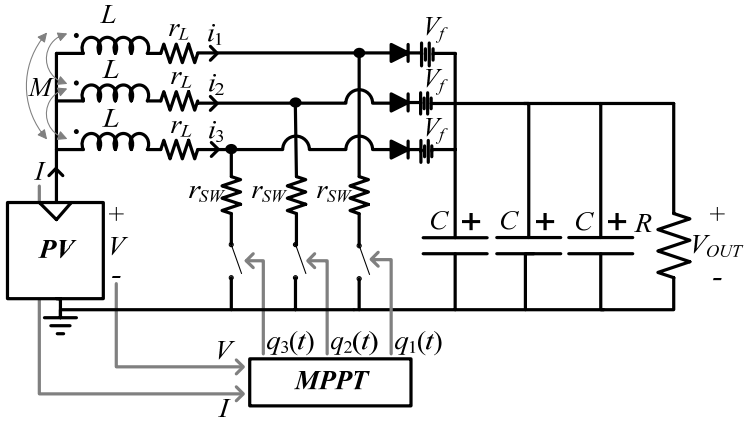


**Figure 2:** Three-phase interleaved boost converter

The model accounts for common conduction losses, including resistive losses in the switching devices, copper losses in the coupled inductor, and forward voltage drops of the diodes. For PV applications, the switch states are determined through an MPPT algorithm that attempts to maximize the power output of the PV module. Ripple correlation control is chosen to perform the MPPT function owing to its simplicity and ease of implementation. The concept of interleaved switching is illustrated for the three-phase converter in Figure 3. In general, for an *N*-phase converter, the switching commands are delayed by ($2\pi/N$) radians over a switching period *T*.

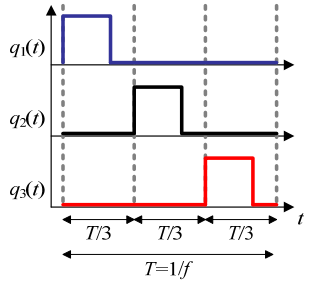


**Figure 3:** Interleaved switching scheme for a three-phase converter

## 2.2 Photovoltaic Module Model

The physics-based model of a solar cell is shown in Figure 4 [28]-[30]. The current sourced ($I_{SC}$) is proportional to the amount of incident insolation while the parameters of the diode and the value of the resistances are a function of the fabrication process. Figure 5 depicts how a conventional PV module is built with several such cells connected in series to augment the module voltage, and series strings connected in parallel to increase the current.

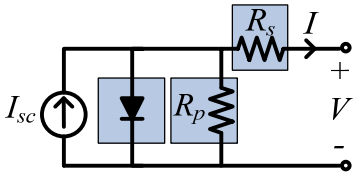


**Figure 4:** Solar cell model

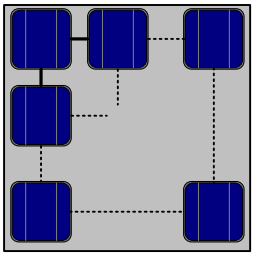

**Figure 5:** Cells connected to form a PV module

In practice, it is difficult to obtain parameters to model the shaded components (with reference to Figure 4). Data sheets of PV modules generally do not provide detailed information about the parameters of the solar cells or their layout in the module. To circumvent these impediments, [31] proposes the following description for the PV module current:

$$I = I_{SC}\left[1 - C_1\left(e^{\frac{V}{C_2 V_{OC}}}\right) - 1\right] \tag{1}$$

In (1), the constants $C_1$ and $C_2$ are defined as

$$C_1 = \left(1 - \frac{I_M}{I_{SC}}\right) e^{\left(\frac{-V_M}{C_2 V_{OC}}\right)} \tag{2}$$

$$C_2 = \frac{\frac{V_M}{V_{OC}} - 1}{\ln\left(1 - \frac{I_M}{I_{SC}}\right)} \tag{3}$$

The PV current and voltage are denoted as $I$ and $V$ respectively. The subscripts $M$, $OC$ and $SC$ refer to maximum, open circuit and short circuit, respectively. The maximum current and voltage, short-circuit current, and open-circuit voltage are readily available in data sheets of PV modules. For completeness, these quantities are corrected for solar insolation and ambient temperature, different from the standard test condition (STC) values of 1000 W/m$^2$ and 25$^o$C, respectively. The correction procedure is captured in (4)-(9), where the values of current and voltage parameters at $S_{STC}$=1000 W/m$^2$ and $T_{STC}$=25 $^o$C are additionally qualified using the subscript $STC$:

$$\Delta T = T - T_{STC} \tag{4}$$

$$\Delta S = \left(\frac{S}{S_{STC}}\right) - 1 \tag{5}$$

$$I_{SC} = I_{SC-STC}\left(\frac{S}{S_{STC}}\right) + \alpha \Delta T \tag{6}$$

$$I_M = I_{M-STC}\left(\frac{S}{S_{STC}}\right) + \alpha \Delta T \tag{7}$$

$$V_{OC} = (V_{OC-STC} - \beta \Delta T)\ln(e + \gamma \Delta S) \tag{8}$$

$$V_M = (V_{M-STC} - \beta \Delta T)\ln(e + \gamma \Delta S) \tag{9}$$

As an example, an SPR-230-WHT PV module is adopted here [32], with the parameters extracted and summarized in Table 1. The variation in the open-circuit voltage due to incident insolation is not accounted for, as the coefficient that captures this change is not available in the data sheet. The variation of the *I-V* curve for this module under varying insolation and temperature is depicted in Figure 6.

TABLE 1
PARAMETERS OF PV MODULE: SPR-230-WHT [32]

| Symbol | Quantity | Value |
|---|---|---|
| $V_{OC\text{-}STC}$ | Rated open-circuit voltage | 48.7 V |
| $I_{SC\text{-}STC}$ | Rated short-circuit current | 5.99 A |
| $I_{M\text{-}STC}$ | Rated current | 5.61 A |
| $V_{M\text{-}STC}$ | Rated voltage | 41 V |
| $P_{M\text{-}STC}$ | Rated power | 230.01 W |
| $\alpha$ | Temperature coefficient for current | 3.5 mA / $^{o}$C |
| $\beta$ | Temperature coefficient for voltage | -132.5 mV / $^{o}$C |
| $\gamma$ | Insolation coefficient for voltage | 0 |
| $S_{STC}$ | Nominal incident insolation | 1000 W/m$^2$ |
| $T_{STC}$ | Nominal ambient temperature | 25 $^{o}$C |

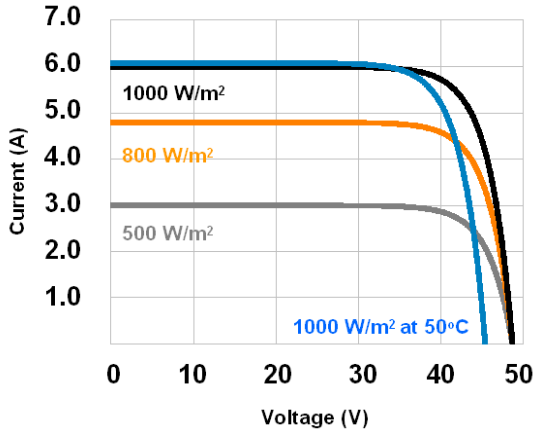


**Figure 6:** Simulated *I-V* curves of SPR-230-WHT module

To demonstrate the necessity of maximum power point tracking, consider Figures 7-8, referenced to the SPR-230-WHT module. Figure 7 illustrates the variation of the available power from the PV module as a function of the incident insolation and terminal voltage. Notice that for each value of insolation, there is a unique terminal voltage that yields maximum power. Similar hill-shaped characteristics would be obtained by plotting the PV power as a function of module voltage and ambient temperature. Figure 8 depicts the variation of the maximum power output of the panel as a function of module voltage and incident insolation. Figures 7-8 illustrate the requirement of dc-dc converters to implement the function of extracting the maximum power

from the PV source. These converters operate such that the terminal voltage of the PV module is optimal and guarantee the extraction of maximum power across all possible ambient conditions.

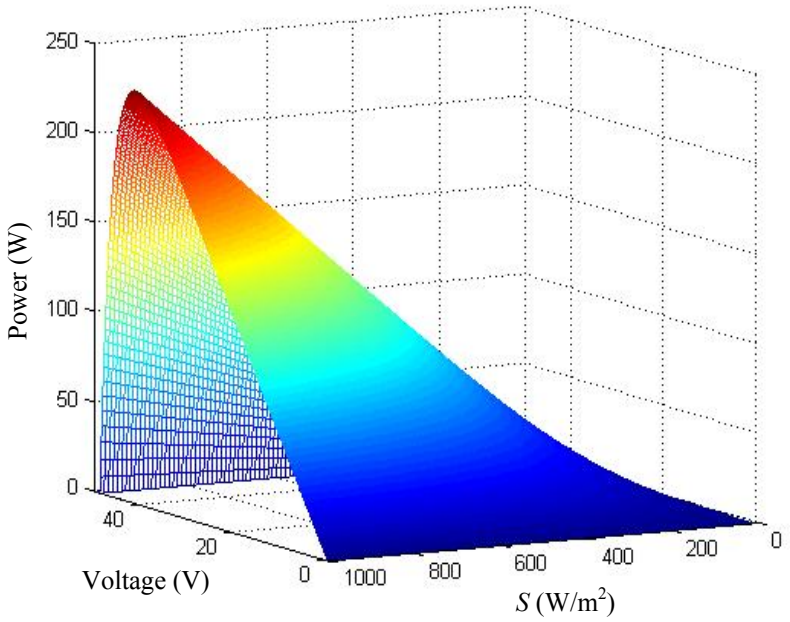


**Figure 7:** PV power as a function of voltage and insolation

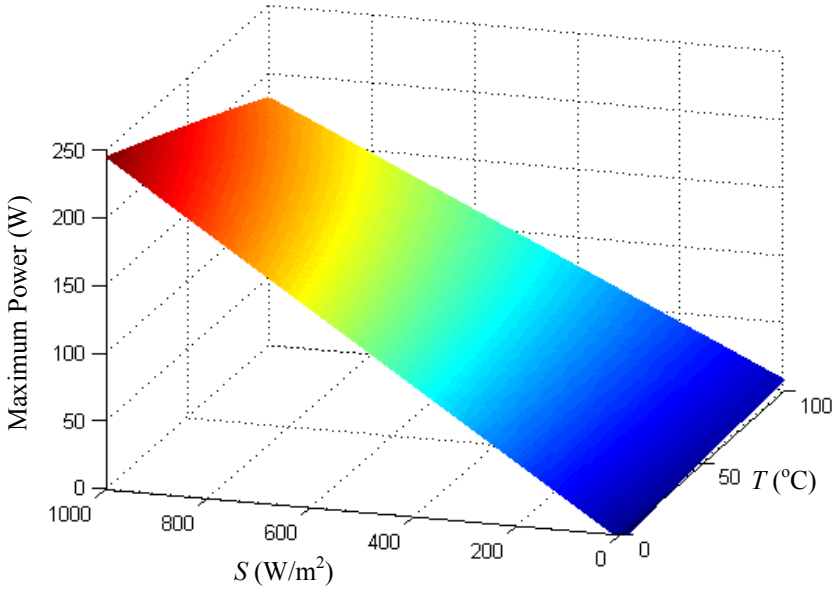


**Figure 8:** Maximum available power as a function of temperature and insolation

## 2.3 Coupled Inductor Model

Research pertaining to simulation tools and to behavioral and physics-based models for coupled inductors can be found in [33]-[34]. A symmetric inductance matrix that captures the most relevant dynamics in coupled inductors is used here.

$$\mathbf{v}(t) = \mathbf{L}\frac{d\mathbf{i}(t)}{dt} + \mathbf{R}\mathbf{i}(t) \tag{10}$$

$$\begin{bmatrix} v_1(t) \\ v_2(t) \\ \dots \\ v_N(t) \end{bmatrix} = \begin{bmatrix} L_1 & M_{12} & .. & M_{1N} \\ M_{12} & L_2 & .. & M_{2N} \\ .. & .. & .. & .. \\ M_{1N} & M_{2N} & .. & L_N \end{bmatrix} \frac{d}{dt} \begin{bmatrix} i_1(t) \\ i_2(t) \\ \dots \\ i_N(t) \end{bmatrix} + \begin{bmatrix} r_{L_1} & 0 & 0 & 0 \\ 0 & r_{L_2} & 0 & 0 \\ 0 & 0 & .. & 0 \\ 0 & 0 & 0 & r_{L_N} \end{bmatrix} \begin{bmatrix} i_1(t) \\ i_2(t) \\ \dots \\ i_N(t) \end{bmatrix} \tag{11}$$

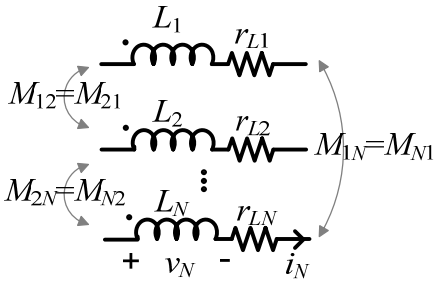


**Figure 9:** *N*-winding coupled inductor schematic

As depicted in Figure 9, $L_i$ represents the self-inductance and $r_{Li}$ represents the winding resistance of phase $i$. The coupling between phases $i$ and $j$ is captured by mutual inductance $M_{ij}$. While the expressions in (10)-(11) capture the most relevant dynamic behavior of $N$-winding coupled inductors, effects such as saturation and eddy currents are disregarded. In the proposed application, we utilize a relatively low switching frequency which renders copper loss more dominant when compared to core loss. Additionally, it is assumed that the magnetic design avoids saturation under all operating conditions. A detailed procedure for designing filter inductors and isolation transformers applicable to power-electronic applications is available in [35].

## 2.4 Maximum Power Point Tracking using Ripple Correlation Control

Innumerable techniques to track the maximum power point of a PV array are documented in the literature (see [36]-[39] and references therein for recent work in this area). A comparison of the most widely used classes of MPPT techniques is given in [40]. In this work, the MPPT algorithm is implemented using ripple correlation control (RCC) [41]-[43]. RCC utilizes voltage and current ripple, inherently present in switch-mode power converters to maximize the power

out of a PV array [44]-[45]. The algorithm is inherently robust and offers simple hardware implementation. For a boost converter, the RCC law that governs the variation of the active switch duty ratio, $D_{SW}(t)$ is given by:

$$D_{SW}(t) = -k\int\left(\frac{dP}{d\tau}\right)\left(\frac{dV}{d\tau}\right)d\tau \tag{12}$$

The PV power and voltage are expressed as $P$ and $V$ respectively; $k$ is a positive constant that ensures the power gradient is driven to zero upon applying the control law, and its magnitude affects the transient performance of the algorithm. Implementation issues in RCC, limitations, optimal choice of constants and suggested practices are well discussed in [44].

## 2.5 Photovoltaic System Performance

Estimating the energy produced by the PV source is critical to reliability metrics derived subsequently. In this section, certain pertinent concepts that deal with estimating PV system performance are presented.

### 2.5.1 Peak-hours approach [46]

The available solar energy is a strong function of incident insolation and ambient temperature. The incident insolation is defined as the power available per unit area and denoted as $S$. Generally, estimated average insolations are defined in terms of energy available per unit area per day. We denote this quantity as $E$. Tables such as Table 2 (from [46]) are widely used as a first step in determining the area of collector needed and effects of tilt angle and seasonal variations on harvestable photovoltaic energy.

TABLE 2 [46]:

RADIATION DATA [E (KWH/M$^2$DAY)] FOR LOS ANGELES, CA

| Tilt | Jan | Feb | Mar | Apr | May | Jun | Jul | Aug | Sep | Oct | Nov | Dec | Year |
|---|---|---|---|---|---|---|---|---|---|---|---|---|---|
| L-15$^o$ | 3.8 | 4.5 | 5.5 | 6.4 | 6.4 | 6.4 | 7.1 | 6.8 | 5.9 | 5.0 | 4.2 | 3.6 | 5.5 |
| L | 4.4 | 5.0 | 5.7 | 6.3 | 6.1 | 6.0 | 6.6 | 6.6 | 6.0 | 5.4 | 4.7 | 4.2 | 5.6 |
| L+15$^o$ | 4.7 | 5.1 | 5.6 | 5.9 | 5.4 | 5.2 | 5.8 | 6.0 | 5.7 | 5.5 | 5.0 | 4.5 | 5.4 |
| 90$^o$ | 5.1 | 4.1 | 3.8 | 3.3 | 2.5 | 2.2 | 2.4 | 3.0 | 3.6 | 4.2 | 4.3 | 4.1 | 3.5 |
| Temp. ($^o$C) | 18.7 | 18.8 | 18.6 | 19.7 | 20.6 | 22.2 | 24.1 | 24.8 | 24.8 | 23.6 | 21.3 | 18.8 | 21.3 |

L-Latitude, Tilt-angle off the ground at which the PV array is installed

The peak-hours approach provides a convenient method to interpret the average insolation numbers. Under this methodology, the term "one sun" of insolation is defined to be equal to 1 kW/m$^2$. For instance, from the radiation data for Los Angeles presented in Table 2, for a PV installation tilted at 90$^o$, it is specified that the average value of $E$ is 3.5 kWh/m$^2$day. Hence, it can be surmised that the site receives one sun insolation for 3.5 hours per day on average at an angle of 90$^o$ from horizontal. For a given installation, the energy harvested per day can then be expressed as

$$Energy\left(\frac{\text{kWh}}{\text{day}}\right) = E\left(\frac{\text{kWh}}{\text{m}^2\text{day}}\right) A(\text{m}^2)\eta_{AVG} \tag{13}$$

In (13), $A$ is the area of the PV array and $\eta_{AVG}$ is the efficiency of the energy-conversion process, averaged over the period of a day. Assuming that the PV source is exposed to one sun of insolation, the power available can be expressed as:

$$P(kW) = (\text{one sun})A(\text{m}^2)\eta_{\text{one sun}} = 1\left(\frac{\text{kW}}{\text{m}^2}\right) A(\text{m}^2)\eta_{\text{one sun}} \tag{14}$$

The power harvested by the switch-mode power converter is denoted as $P$, with efficiency under one-sun conditions expressed as $\eta_{one\ sun}$. The area of the modules is eliminated from (14) by appropriately substituting (13) to obtain

$$Energy\left(\frac{\text{kWh}}{\text{day}}\right) = \frac{P(\text{kW})}{1\left(\frac{\text{kW}}{\text{m}^2}\right)} E\left(\frac{\text{kWh}}{\text{m}^2\text{day}}\right) \frac{\eta_{AVG}}{\eta_{\text{one sun}}} \tag{15}$$

Assuming that the average and one-sun efficiencies are similar, the energy harvest per day can be expressed as:

$$Energy\left(\frac{\text{kWh}}{\text{day}}\right) = P(\text{kW})\left(\frac{\text{h}}{\text{day}}\right)_{\text{one sun}} \tag{16}$$

That is, the energy available per day is the product of the rated power of the system and the hours per day of peak sun.

As an example, consider a south facing 5 kW PV system installed at Los Angeles, CA, with a tilt angle equal to 18.93$^o$ (Latitude-15$^o$). Table 2 indicates that the average energy yield per day per unit area is equal to 5.5 kWh/m$^2$day. That is,

$$E = 5.5\left(\frac{\text{kWh}}{\text{m}^2\text{day}}\right) \tag{17}$$

Note that this can be interpreted as 5.5 hours per day of one-sun insolation on average. For the 5 kW system, the average energy yield per day follows from (16) as

$$Energy = 5.5\left(\frac{\text{h}}{\text{day}}\right)_{\text{one sun}} 5(\text{kW}) = 27.5\left(\frac{\text{kWh}}{\text{day}}\right) \tag{18}$$

### 2.5.2 Capacity factor

With reference to PV installations, the capacity factor, *CF*, describes the fraction of a year over which the PV source delivers rated power. For instance, an installation is said to have a capacity factor of 50% if it delivers its rated power for 50% of the time in a year. There is a fair amount of ambiguity in the definition of the capacity factor, as it could also be summarized that the PV installation always delivers 50% of the rated power. The energy harvest per year (notice that (13) defines the energy harvest per day) can then be expressed as

$$Energy\left(\frac{\text{kWh}}{\text{year}}\right) = P(\text{kW})8760\left(\frac{\text{h}}{\text{year}}\right)CF \tag{19}$$

Combining (16) and (19) yields an alternate expression for the capacity factor,

$$CF = \frac{\left(\frac{\text{h}}{\text{day}}\right)_{\text{one sun}}}{24\left(\frac{\text{h}}{\text{day}}\right)} \tag{20}$$

Thus, the capacity factor can be expressed as the fraction of the day over which one-sun insolation is received.

# CHAPTER 3

## STEADY-STATE OPERATION OF *N*-PHASE BOOST CONVERTER

A brief overview of the switching configurations of the multiphase converter is presented, followed by the theoretical analysis to describe the converter's steady-state operation.

### 3.1 Switching Configurations

The steady-state operation of the *N*-phase interleaved boost converter will be examined in the context of a three-phase, interleaved converter. The schematic of this topology was highlighted in Figure 2. The switching states corresponding to one period are documented in Table 3. It is assumed that all three phases are operating with the same duty ratio. The variable $SW_i$ refers to the active switch and $D_i$ refers to the diode in phase $i$. The generic current waveforms for a three-phase converter are shown in Figure 10 wherein the periods described in the table below are marked.

TABLE 3
SWITCH STATES OF THREE-PHASE CONVERTER IN ONE PERIOD

| Period | $SW_3$ | $SW_2$ | $SW_1$ | $D_3$ | $D_2$ | $D_1$ |
|---|---|---|---|---|---|---|
| *A* | ON | OFF | OFF | OFF | OFF | ON |
| *B* | ON | OFF | OFF | OFF | OFF | OFF |
| *C* | OFF | OFF | OFF | ON | OFF | OFF |
| *D* | OFF | ON | OFF | ON | OFF | OFF |
| *E* | OFF | ON | OFF | OFF | OFF | OFF |
| *F* | OFF | OFF | OFF | OFF | ON | OFF |
| *G* | OFF | OFF | ON | OFF | ON | OFF |
| *H* | OFF | OFF | ON | OFF | OFF | OFF |
| *I* | OFF | OFF | OFF | OFF | OFF | ON |

Some general trends of operation are highlighted below:

- Each individual phase operates in discontinuous current mode (DCM). However, the sum of the currents, which equals the current drawn from the panel, will always be continuous.
- It can be shown that the difference in the average currents in the different phases is directly proportional to the difference in duty ratio of the corresponding active switches. This difference can be reduced by increasing the self-inductance of the phases [17].
- Strongly coupled inductors with relatively small leakage inductance terms will ensure that the periods *A*, *D*, *G*, etc. (with reference to Figure 10), are very short, which can aid in reducing the PV current ripple.

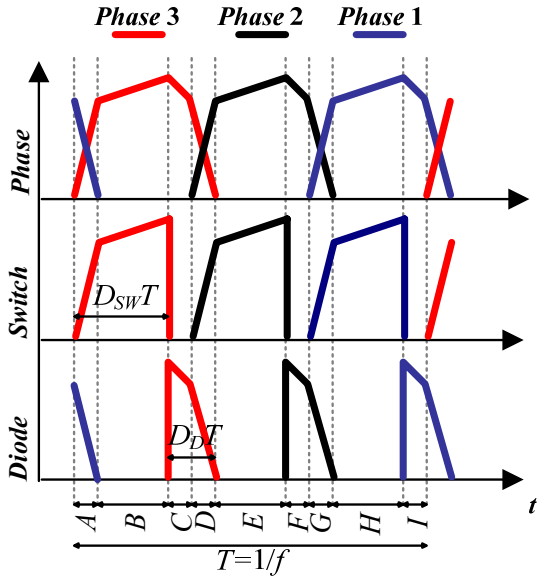


**Figure 10:** Current waveforms for a three-phase converter

## 3.2 Steady-State Characterization

To simplify the forthcoming analysis, it is assumed that each phase is equally coupled with every phase. Hence, the inductance matrix has the following structure:

$$\mathbf{L} = \begin{bmatrix} L & M & .. & M \\ M & L & .. & M \\ .. & .. & .. & .. \\ M & M & .. & L \end{bmatrix}_{NxN} \tag{21}$$

The expressions for the output voltage, peak-to-peak output-voltage ripple, and peak-to-peak input-current ripple derived below provide a bound on the quantities they describe if the above simplification is not valid.

### 3.2.1 Output voltage

In steady state, the MPPT block ensures that the terminal voltage and current of the module are $V_M$ and $I_M$ respectively. Imposing charge-second balance for the capacitors,

$$N \int_{D_DT} (I_M - V_{OUT}/R)dt + N \int_{D_{SW}T} (-V_{OUT}/R)dt = 0 \tag{22}$$

Expanding the above integral,

$$\left(I_M - V_{OUT}/R\right)D_D - \left(V_{OUT}/R\right)D_{SW} = 0 \tag{23}$$

From the current waveforms in Figure 11 on page 19, notice that each phase shares the PV current equally in an average sense. To ensure energy balance, this requires:

$$D_{SW} + D_D = 1/N \tag{24}$$

To obtain the last equation to solve for $D_{SW}$, $D_D$, and $V_{OUT}$ we consider the power balance in the circuit,

$$P_{IN} = P_{OUT} + P_{LOSS} \tag{25}$$

The losses in the circuit are the sum of copper loss in the coupled inductors, $P_L$, resistive losses in the switches, $P_{SW}$, and losses due to the forward voltage drop of the diodes, $P_D$.

$$V_M I_M = V_{OUT}^2/R + P_L + P_{SW} + P_D \tag{26}$$

Given the assumptions of strong coupling and sufficiently large self-inductance, each individual phase carries approximately the entire PV current, $I_M$, when either the active switch or diode conducts. Otherwise, the phase current is zero. Based on this observation, we can appropriately substitute for the losses in (26) to yield the following:

$$V_M I_M = V_{OUT}^2/R + {I_M}^2 r_L + NI_M^2 r_{SW} D_{SW} + NI_M V_f D_D \tag{27}$$

Substituting for $V_{OUT}$ from (23) and $D_D$ from (24) in (27) provides the following quadratic equation in the switch duty ratio, $D_{SW}$:

$$D_{SW}^2[N^2 I_M^2 R] + D_{SW}[NI_M^2 r_{SW} - NI_M V_f - 2NI_M^2 R] + [I_M^2 R - I_M V + I_M^2 r_L + I_M V_f] = 0 \tag{28}$$

The above equation yields two values of $D_{SW}$. We neglect the solution greater than 50% given the knowledge of converter operation (24). Equation (29) then provides the following expression for the output voltage:

$$V_{OUT} = I_M R(1 - D_{SW} N) \tag{29}$$

### 3.2.2 Output voltage ripple

Consider the current through the capacitor bank, which is composed of $N$ capacitors, each with capacitance, $C$:

$$i_C(t) = NC\frac{dV_{OUT}}{dt} \tag{30}$$

Approximating the capacitor current during the period $D_D T$ with a straight-line fit for the output voltage provides the following expression. The current through the capacitor bank is approximated as the difference between the PV current $I_M$, and the load current:

$$I_M - \frac{V_{OUT}}{R} = NC\frac{\Delta V_{OUT}}{D_D T} \tag{31}$$

Isolating the output voltage ripple,

$$\Delta V_{OUT} = \left( I_M - \frac{V_{OUT}}{R} \right) \frac{D_D T}{NC} \tag{32}$$

### 3.2.3 Input current ripple

To simplify the analysis, it is assumed that the converter is lossless. The inverse of the inductance matrix, $\mathbf{L}$, provides the inverse inductance matrix, $\mathbf{\Gamma}$:

$$\mathbf{\Gamma} = \frac{1}{L_{eff}(L - M)} \begin{bmatrix} L + (N-2)M & -M & .. & -M \\ -M & .. & .. & -M \\ .. & .. & .. & .. \\ -M & -M & .. & L + (N-2)M \end{bmatrix} \tag{33}$$

where $L_{eff}$ is defined as

$$L_{eff} = \frac{L^2 + (N-2)LM - (N-1)M^2}{L - M} \tag{34}$$

The time derivative of the panel current can be expressed as the sum of the derivatives of individual phase currents:

$$\frac{dI(t)}{dt} = \sum_{k=1}^{N} \frac{di_k(t)}{dt} \tag{35}$$

Using $\Gamma$, the derivative of the input current also satisfies:

$$\sum_{k=1}^{N} v_k(t) = \frac{L^2 + (N-2)LM - (N-1)M^2}{L - M} \frac{dI(t)}{dt} = L_{eff} \frac{dI(t)}{dt} \tag{36}$$

In the above expression, $v_k(t)$ refers to the voltage across the $k^{\text{th}}$ inductor in the coupled inductor. The voltage across the coupled inductors during any period $D_D T$ is approximately $(V_{OUT} - V_M)$. Thus, (35) can be evaluated using a straight-line fit for the inductor current during $D_D T$:

$$N\left(V_{OUT} - V_M\right) = L_{eff} \frac{\Delta I}{D_D T} \tag{37}$$

Isolating the current ripple and substituting for $L_{eff}$,

$$\Delta I = \frac{N\left(V_{OUT} - V_M\right) D_D T}{L^2 + (N-2)ML - (N-1)M^2} (L - M) \tag{38}$$

We have thus proposed analytical expressions to quantify the output voltage, output voltage ripple, power losses and input current ripple in a *N*-phase, interleaved boost converter interfaced with a PV array. The expressions derived allow for rapid evaluation of converter performance over a wide range of ambient conditions and converter specifications.

### 3.3 Simulation Studies

To validate the analytical, steady-state model of the converter, we consider a three-phase converter, with specifications listed in Table 4. A three-phase interleaved converter model is

developed in Dymola for the PV module described in Table 1. The validity of the model is verified over the insolation range, 200 – 1000 W/m$^2$ at ambient temperatures of 25 $^o$C and 50 $^o$C. The results are given in Figures 11-18. In each case, the theoretical results are plotted as continuous lines (-) and the data points from the simulations are represented as circles (**o**).

TABLE 4
CONVERTER SPECIFICATIONS

| Symbol | Quantity | Value |
|---|---|---|
| $L$ | Self inductance of coupled inductor | 1.2 mH |
| $M$ | Mutual inductance of coupled inductor | 1.18 mH |
| $r_L$ | Winding resistance of each phase | 0.1 Ω |
| $r_{SW}$ | Drain-source ON state switch resistance | 0.1 Ω |
| $V_f$ | Forward voltage drop of diode | 1 V |
| $C$ | Output capacitance | 4.7 µF |
| $R$ | Output load | 50 Ω |
| $f$ | Switching frequency | 10 kHz |

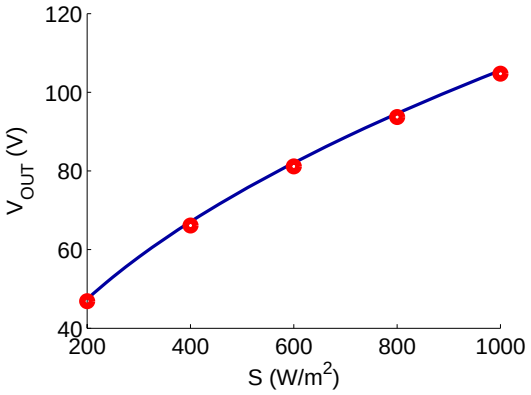


**Figure 11:** Output voltage vs. insolation, 25 $^o$C

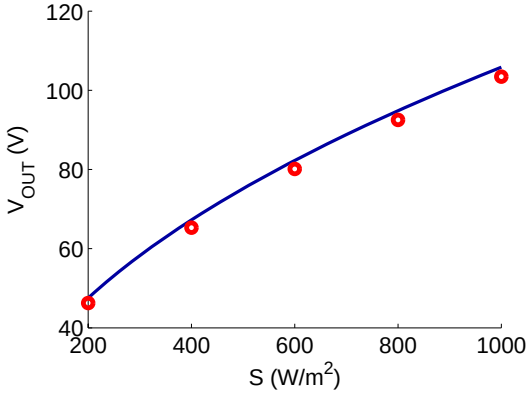


**Figure 12:** Output voltage vs. insolation, 50 $^o$C

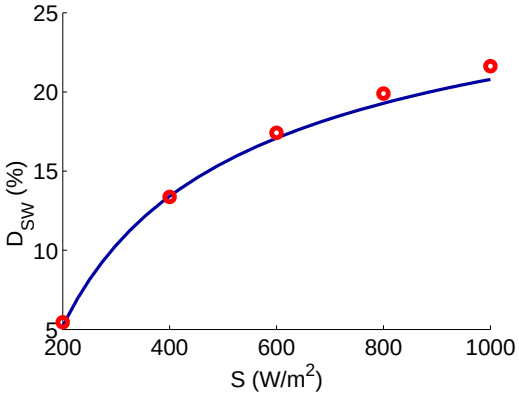


**Figure 13:** Switch duty cycle vs. insolation, 25 $^o$C

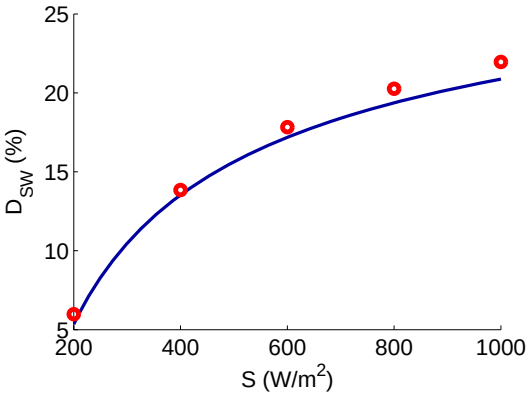


**Figure 14:** Switch duty cycle vs. insolation, 50 $^o$C

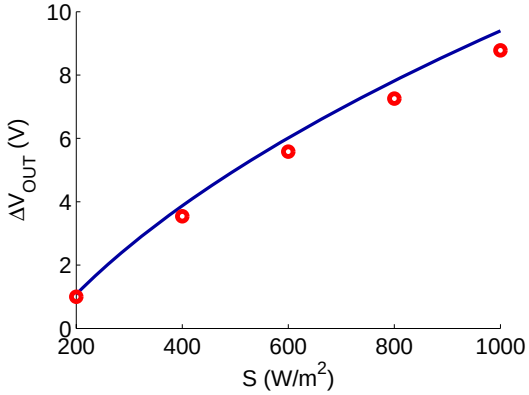


**Figure 15:** Voltage ripple vs. insolation, 25 °C

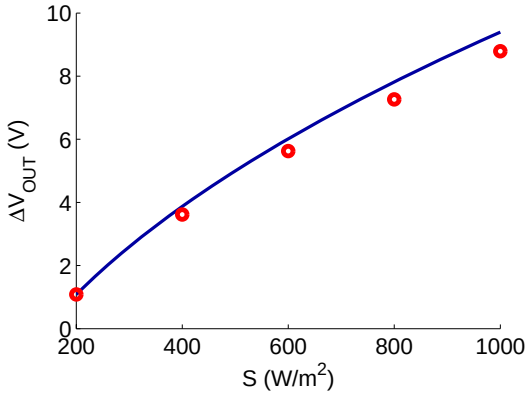


**Figure 16:** Voltage ripple vs. insolation, 50 °C

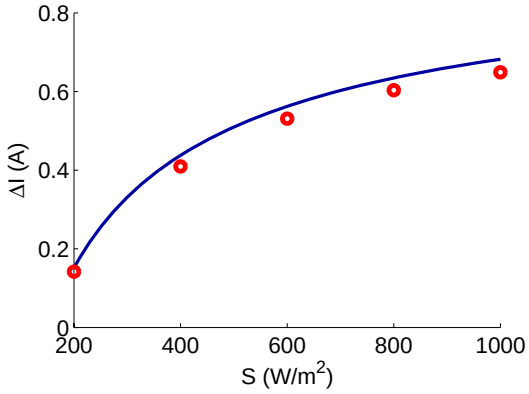


**Figure 17:** Input-current ripple vs. insolation, 25 °C

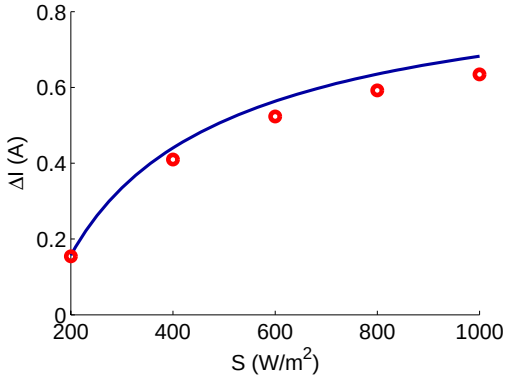


**Figure 18:** Input-current ripple vs. insolation, 50 °C

The analytical models developed for the converter estimate the steady-state operation accurately over a wide range of ambient conditions. The percentage error is no more than 3% for the output voltage, and 7% for the output-voltage and input-current ripple. The maximum difference in the predicted and measured duty cycle is less than 2%. In each case, discrepancies are due to the simplifying assumptions made in the analysis.

### 3.4 Design Strategies and Inferences from Steady-State Model

Several inferences about converter operation and design strategies can now be formulated based on assessing the operation of the converter over a wide spectrum of ambient conditions.

*Output Voltage Ripple*: Figure 19 depicts the variation in voltage ripple with ambient temperature, $T$, and incident insolation, $S$, for converters with different phases, $N$, and output capacitances, $C$. For the same capacitance, a three-phase converter provides lower voltage ripple than its two-phase counterpart. The surfaces (■) and (■) correspond to equal net capacitance ($NC$)

for both converters (two- and three-phase respectively). The voltage ripple in the three-phase converter is still lower than the two-phase converter.

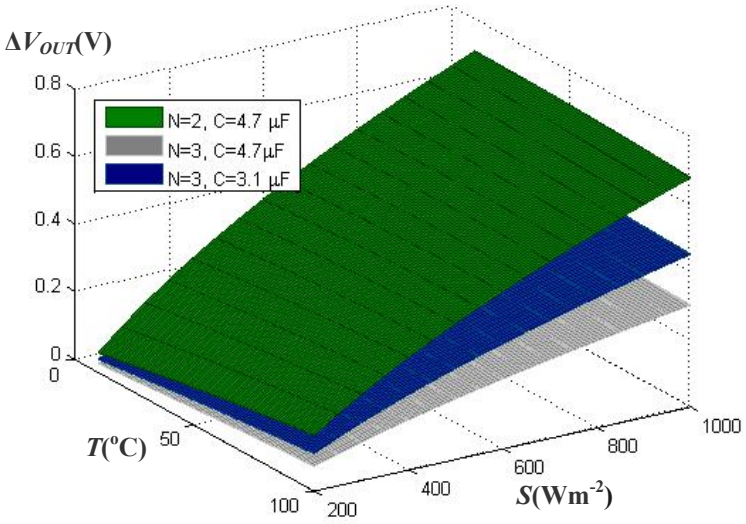


**Figure 19:** Output voltage ripple for different converter specifications

*Panel Current Ripple*: The PV-current ripple for different inductance values in a two-phase and three-phase converter are depicted in Figure 20. The same value of inductance with increased number of phases guarantees lower current ripple across all ambient conditions.

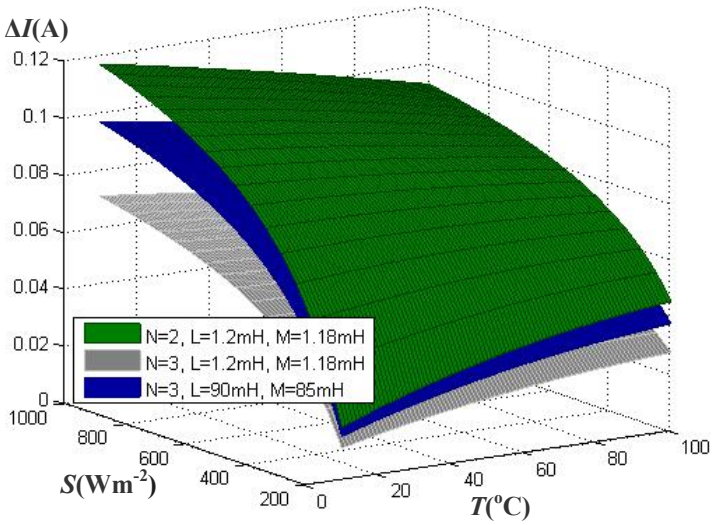


**Figure 20:** PV-current ripple for different converter specifications

*Efficiency*: The converter efficiency is evaluated as the fraction of input power delivered to the output load, with the PV module operating at the maximum power point.

$$\eta = \frac{P_{OUT}}{P_{IN}} = \frac{V_{OUT}^2}{R} \frac{1}{V_M I_M} \tag{39}$$

In terms of the losses in the converter,

$$\eta = \frac{P_{OUT}}{P_{IN}} = \frac{P_{IN} - P_{LOSS}}{P_{IN}} = 1 - \frac{P_{LOSS}}{V_M I_M} \tag{40}$$

The losses are due to conduction losses in the switches, winding resistance in the coupled inductor and the forward voltage drop in the diodes,

$$P_{LOSS} = P_L + P_{SW} + P_D \tag{41}$$

For an *N*-phase converter, these can be expressed as

$$P_L = NI^2 r_L (D_D + D_{SW}) = I^2 r_L \tag{42}$$

$$P_{SW} = NI^2 r_{SW} (D_{SW}) \tag{43}$$

$$P_D = NIV_f D_D \tag{44}$$

As the number of phases increases, the values of $D_{SW}$ and $D_D$ decrease proportionally. Hence, if the switch resistance and the diode drops are the same, we do not expect to see any variation in efficiency by switching to a converter with more phases. This is illustrated in Figure 21, which depicts the efficiency of a three-phase and two-phase converter (both converters with identical specifications attached in Table 4) over a wide range of possible operating conditions. The surfaces corresponding to both cases are noted to overlap.

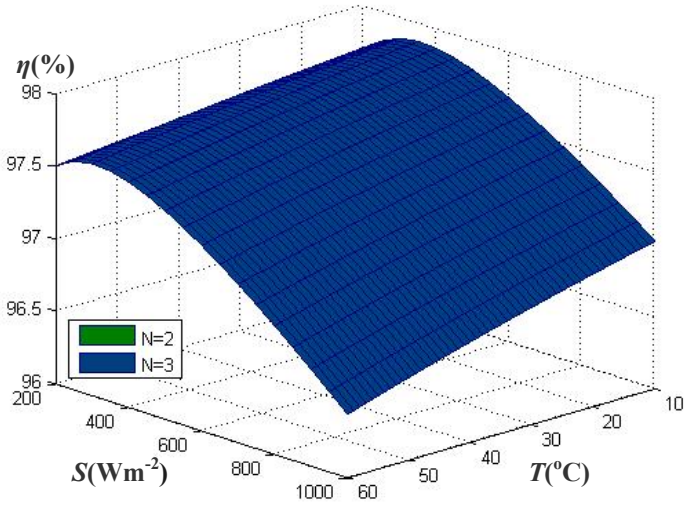


**Figure 21:** Converter efficiency for different phases

It is instructive to assess the dominant losses under different conditions. Consider the various sources of loss for a three-phase converter plotted in Figure 22. At lower values of insolation, the losses due to the diode dominate. At higher values of insolation, the losses due to the inductor and switches creep up. Notice that the losses are practically invariant with operating temperature.

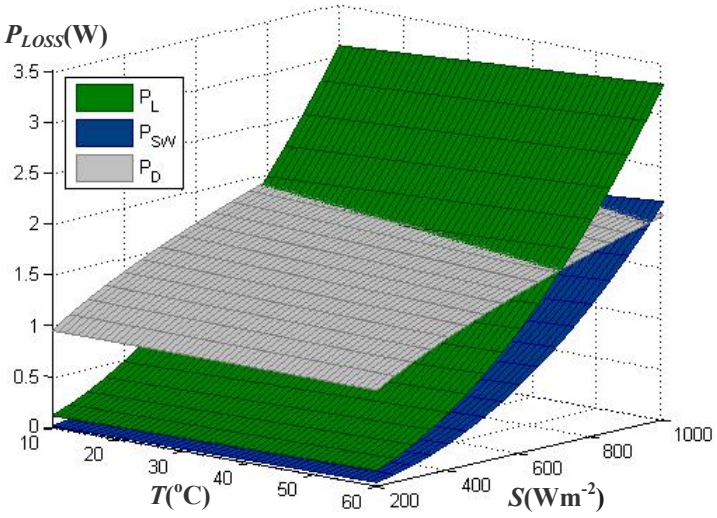


**Figure 22:** Sources of loss compared

# CHAPTER 4

## SYSTEM RELIABILITY ASSESSMENT FRAMEWORK

A bottom-up approach is adapted to evaluate the reliability of the multiphase converter. The component failure rates are estimated based on the widely adopted Military Handbook for Reliability Prediction of Electronic Equipment, MIL-HDBK-217F [47]. The failure rates, albeit constant, are noted to be functions of the operational conditions and number of phases in the converter. This nullifies the possibility of utilizing combinatorial approaches such as reliability block diagrams and fault trees for analysis and necessitates the formulation of a Markov reliability model to evaluate the reliability of the converter. A generic state-transition diagram to describe the reliability of an *N*-phase converter is drafted and the Chapman-Kolmogorov equations are derived and solved to estimate the reliability of the converter. The applicability of the proposed tools is demonstrated in the context of two- and three-phase converters.

### 4.1 Component Failure Rates

The time-invariant rates proposed in [47], can be modeled by exponential probability-density functions. This is not an oversimplification, as large classes of electronic devices are predicted to fail with a constant failure rate over their lifetime. Figure 23 depicts the failure rate of a hypothetical electronic-circuit component over the period of its lifetime. This curve is aptly referred as the "bathtub" curve given the structural similarities it shares with its real-world namesake. The failure rate is initially very high (representative of infant mortality) and settles to a constant value over the useful life period before rising again towards the end of its stipulated lifespan.

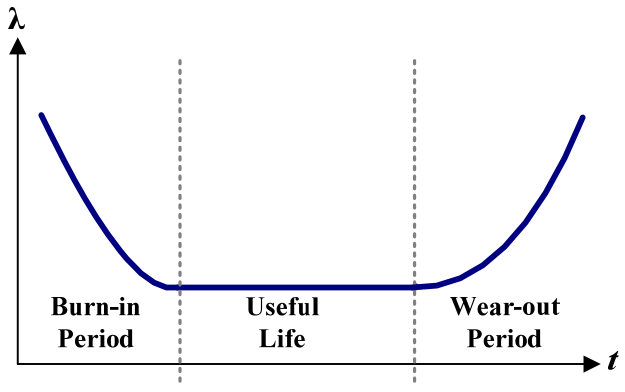


**Figure 23:** Bathtub-shaped failure-rate model

By adapting constant failure rates to characterize the failure of electronics components, we assume that initial weeding has filtered out the infant-mortality phase and that for all practical purposes, the intended system lifetime is longer than the useful lifetime of the component. Most failure rates in [47] are of the general form

$$\lambda_P = \lambda_B \pi_E \pi_Q \prod_i \pi_i \tag{45}$$

where $\lambda_P$ is the part failure rate, $\lambda_B$ is the base failure rate and $\pi_E$ and $\pi_Q$ are modifiers to account for environmental and qualitative effects. If not explicitly stated, the environmental factor is equal to 0.6 for ground-based, immobile applications. Other device-specific modifiers are denoted as $\pi_i$.

To capture the reliability function of a component, begin by defining a continuous-time random variable, $T$, which denotes the time to failure of the component. The reliability and unreliability functions ($R(t)$ and $Q(t)$ respectively) can then be expressed as

$$R(t) = \Pr\{T > t\} \tag{46}$$

$$Q(t) = \Pr\{T \le t\} \tag{47}$$

In other words, at any given time instant $t$, the reliability of the component is the probability that it lasts beyond the instant and the unreliability is simply the probability that the component has failed before the instant.

The probability that the component fails in time $t + \Delta t$ , given that it has survived to time $t$, can be expressed in terms of the failure rate as

$$\Pr\{T \le t + \Delta t \mid T > t\} = \lambda \Delta t \tag{48}$$

The conditional probability of event $A$ given $B$ (where $B$ occurs with non-zero probability) over a defined probability space is expressed using the well-known formula:

$$\Pr(A \mid B) = \frac{\Pr(A \cap B)}{\Pr(B)} \tag{49}$$

Employing this definition to simplify (48):

$$\begin{aligned}\lambda &= \frac{1}{\Delta t}\frac{\Pr\{T \le t+\Delta t \mid T > t\}}{\Pr\{T \ge t\}} \\ &= \frac{1}{\Delta t}\frac{\Pr\{t \le T \le t+\Delta t\}}{\Pr\{T > t\}} \\ &= \frac{1}{\Delta t}\frac{\Pr\{T \le t+\Delta t\} - \Pr\{T \le t\}}{\Pr\{T > t\}} \\ &= \frac{1}{\Delta t}\frac{Q(t+\Delta t) - Q(t)}{R(t)} \\ &= \frac{1}{\Delta t}\frac{-[R(t+\Delta t) - R(t)]}{R(t)} \\ &= \frac{1}{\Delta t}\frac{-\Delta R(t)}{R(t)} \end{aligned} \tag{50}$$

In the limit, for a very small time step $\Delta t$, the failure rate can be described by the differential equation

$$\lambda = \lim_{\Delta t \to 0}\frac{1}{\Delta t}\frac{-\Delta R(t)}{R(t)} = -\frac{1}{R(t)}\frac{dR(t)}{dt} \tag{51}$$

The solution of the above equation for constant, time-invariant failure rates yields the following expressions for the reliability and unreliability function of the component:

$$R(t) = e^{-\lambda t} \tag{52}$$

$$Q(t) = 1 - e^{-\lambda t} \tag{53}$$

Notice that the cumulative distribution function of the random variable, $T$, is the same as the unreliability function, $Q(t)$.

We now document the failure rates of the different components in the multiphase converter. All failure rates in [47] are expressed with units of failures per million hours of operation. The types of devices used in the converter are documented in Table 5.

TABLE 5
COMPONENT CHOICES

| Component | Type |
|---|---|
| Active switches | N-Channel silicon power field effect transistors |
| Diodes | Schottky power diodes |
| Capacitors | Dry aluminum electrolytic capacitors |

### 4.1.1 Capacitors

Dry-electrolytic aluminum capacitors are utilized to realize the output filter in the converter. The failure rate of the capacitors, $\lambda_{CAP}$, is expressed as:

$$\lambda_{CAP} = \lambda_B \pi_{CV} \pi_E \pi_Q \tag{54}$$

In (54), the base failure rate, $\lambda_B$, is a function of the operational voltage stress, $S_{CAP}$ and the ambient temperature, $T$:

$$\lambda_B = 0.0028\left[\left(\frac{S_{CAP}}{0.55}\right)^3 + 1\right]\exp\left(4.09\left(\frac{T + 273\text{K}}{358\text{K}}\right)^{5.9}\right) \tag{55}$$

The operational voltage stress is defined as the ratio of the peak to rated voltage of the capacitor. For the multiphase converter, it can be computed as:

$$S_{CAP} = \left(\frac{V_{OUT} + \Delta V_{OUT}/2}{V_{RATED-CAP}}\right) \tag{56}$$

The capacitance factor, $\pi_{CV}$, derates the failure rate based on the value of capacitance $C$, through the following:

$$\pi_{CV} = 0.32C^{0.19} \tag{57}$$

Lastly, $\pi_E$ and $\pi_Q$ are 2 and 10 for fixed ground-based applications employing non-military grade capacitors.

The effect of the stress factor on the reliability of the capacitors is fairly palpable. All else held constant, the output voltage, $V_{OUT}$, increases with increased insolation. The peak voltage,

$\Delta V_{OUT}/2$, would decrease with increased number of phases $N$. Hence, insolation and number of phases directly affect the failure of the capacitor bank. Note that the effects of temperature are ambivalent. Apart from affecting the base failure rate through the exponential dependence, increased temperature implies decreased PV output and hence decreased output voltage which in-turn implies a decreased stress factor.

### 4.1.2 Diode

Schottky power diodes are employed in the converter, and their failure rate, $\lambda_{DIODE}$, is expressed as:

$$\lambda_{DIODE} = \lambda_B \pi_T \pi_S \pi_C \pi_E \pi_Q \tag{58}$$

The base failure rate, $\lambda_B$, is constant and equal to 0.003 for Schottky devices. The temperature factor, $\pi_T$, is:

$$\pi_T = \exp\left[-3091\left(\frac{1}{T_J + 273\text{K}} - \frac{1}{298\text{K}}\right)\right] \tag{59}$$

The junction temperature, $T_J$, of the diode is evaluated using the expression

$$T_J = T_C + \Theta_{JC} P_D \tag{60}$$

In the above expression, $T_C$ is the device case temperature and $\Theta_{JC}$ is the junction-case thermal resistance of the device. We will assume that the case temperature is 30 $^{o}$C above the ambient, while the junction-case thermal resistance depends on the packaging of the component. Finally, $P_D$ is the power loss in the diode modeled as conduction loss due to the non-zero forward voltage drop. The stress factor, $\pi_S$, accounts for the operational reverse-voltage stress of the diode relative to the rated voltage:

$$\pi_S = \left(\frac{V_{OUT}}{V_{RATED}}\right)^{2.43} \text{ if } 0.3 < \left(\frac{V_{OUT}}{V_{RATED}}\right) \leq 1 \text{ or } \pi_S = 0.054 \text{ if } \left(\frac{V_{OUT}}{V_{RATED}}\right) \leq 0.3 \tag{61}$$

The effect of the physical contact made with the diode on the printed circuit board is captured by the contact construction factor, $\pi_C$. This factor is unity for metallurgical bonded contacts.

Finally, analogous to the case of the active switch, $\pi_Q$ is equal to 8. The stress factor suggests that reliability can be greatly improved by using a diode with a higher voltage rating.

### 4.1.3 Active switch

N-channel silicon power field-effect transistors realize the active switching devices in the converter. The failure rate of the switching devices, $\lambda_{SW}$, is described as:

$$\lambda_{SW} = \lambda_B \pi_T \pi_A \pi_E \pi_Q \tag{62}$$

The base failure rate, $\lambda_B$, is constant and equal to 0.012 for MOSFET devices. The temperature factor, $\pi_T$, depends on the junction temperature, $T_J$, through the following:

$$\pi_T = \exp\left[-1925\left(\frac{1}{T_J + 273\text{K}} - \frac{1}{298\text{K}}\right)\right] \tag{63}$$

The junction temperature of the switch is defined and computed as with the diode (60). The application and quality factors, $\pi_A$ and $\pi_Q$, are 8 (for switches rated at 200 W). The variation of the application factor for MOSFET devices is shown in Table 6.

TABLE 6
VARIATION OF APPLICATION FACTOR WITH SWITCH POWER RATING

| $P_{RATING}$ (W) | $\Pi_A$ |
|---|---|
| $P_{RATING} < 2$ | 1.5 |
| $2 \le P_{RATING} < 5$ | 2 |
| $5 \le P_{RATING} < 50$ | 4 |
| $50 \le P_{RATING} < 250$ | 8 |
| $P_{RATING} \ge 250$ | 10 |

From (62)-(63), it is noted that the incident insolation, number of phases, temperature of operation, power rating and switch losses directly affect MOSFET reliability. The power losses of each switch will be directly proportional to the amount of insolation incident on the panel and inversely proportional to the number of phases. This is because, as the insolation increases, the panel current increases. However, with $N$ phases, the average power handled by each phase is only $1/N$ of the power output of the panel. The effect of ambient temperature on reliability is much more subtle. On one hand, rising temperature will reduce the power output of the panel, reduce the losses, and increase reliability based on the temperature factor. On the other hand,

increased temperatures could possibly worsen reliability as the case temperature is also likely to increase, adversely impacting the temperature factor.

### 4.1.4 Coupled inductor

The coupled inductor arrangement (Figure 10) consists of $N$ coils wound on a single core. For simplicity and a lack of available information on complicated magnetic designs in [47], we assume that the arrangement is analogous to $N$ non-coupled power inductors. The maximum operating temperature of the inductors is assumed to be 125 $^{o}$C, which classifies the insulation as Type B. The failure rate for each coil is given by:

$$\lambda_L = \lambda_B \pi_E \pi_Q \tag{64}$$

The base failure rate, $\lambda_B$, for the Type-B insulation class is:

$$\lambda_B = 0.0018 \exp\left( \frac{T_{HS} + 273\text{K}}{364\text{K}} \right)^{8.7} \tag{65}$$

The hot spot temperature, $T_{HS}$, captures the average temperature increase beyond ambient for the inductor:

$$T_{HS} = T + 1.1\Delta T \tag{66}$$

Methods of varying accuracy are proposed in [47] to estimate the factor $\Delta T$. The failure rate of the inductor is independent of converter design and device ratings. In addition, we have noted that insolation and not temperature is the dominant factor that affects the power sourced by the PV module. However, the only factor that affects the failure rate of the inductor is temperature. For these reasons, the failure of the coupled inductor is neglected in the forthcoming analysis. Similar simplifying assumptions have been characteristic of previous work in related areas.

## 4.2 Variation of Device Failure Rates with Operating Conditions

To demonstrate the key concepts elucidated thus far, we revert to the converter specifications considered in Table 4, with relevant device ratings listed below in Table 7. These ratings apply regardless of the number of phases in the multiphase converters considered subsequently.

TABLE 7
DEVICE RATINGS IN MULTIPHASE CONVERTER

| Symbol | Quantity | Value |
|---|---|---|
| $P_{RATING\text{-}SW}$ | Power rating of active switches | 200 W |
| $r_{SW}$ | Drain-source ON state switch resistance | 0.1 Ω |
| $V_f$ | Forward voltage drop of diode | 1 V |
| $V_{RATING\text{-}DIODE}$ | Voltage rating of diode | 150 V |
| $\Theta_{JC}$ | Junction-case thermal resistance (TO-220 Package) | 5 W/$^o$C |

Based on the description of the failure rates in the previous section, the dominant factors that affect the failure rates of the different components in the converter are insolation, temperature, number of phases and device ratings. It had been noted earlier that the effects of ambient conditions on the failure rates of the components was not readily apparent. Along these lines, the variation of the failure rates with insolation and ambient temperature is probed, with a special emphasis on number of phases and device ratings. This serves as a useful precursor to the discussion on the overall converter reliability.

### 4.2.1 Capacitor

Figure 24 depicts the variation of the capacitor failure rate, $\lambda_{CAP}$, as a function of incident insolation, $S$, and ambient temperature, $T$, for different number of phases, $N$. As $N$ increases, the output voltage ripple decreases, and hence, the failure rates drop across all ambient conditions. A common characteristic that Figure 24 shares with those that follow is the seeming independence of $\lambda_{CAP}$ to temperature except at high insolation levels, and in all cases, the influence of insolation is dominant.

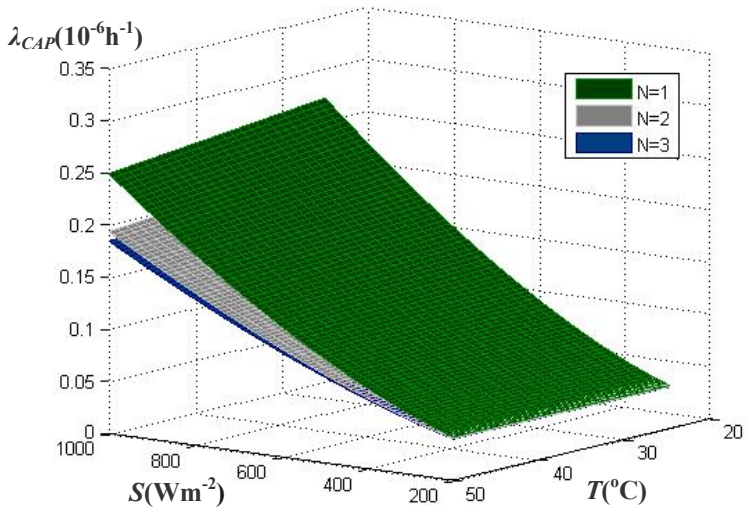


**Figure 24:** Capacitor failure rate as a function of number of phases

Figure 25 assesses the impact of voltage rating and value of capacitance on capacitor reliability for a two-phase converter. Equation (57) indicated that the failure rate is severely degraded with higher value of capacitance and this is evident from the surfaces below. The voltage rating is also noted to play a momentous role in the degradation of the failure rate across all ambient conditions.

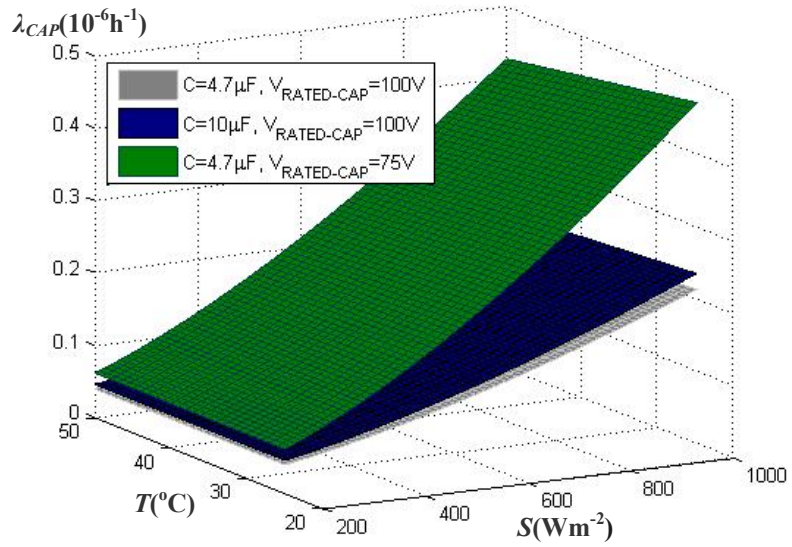


**Figure 25:** Capacitor failure rate as a function of capacitance and voltage rating

Figure 26 depicts the variation of $\lambda_{CAP}$ with switching frequency over a wide range of operational conditions. Notice that a ten-fold increase in switching frequency only marginally improves the reliability of the capacitors.

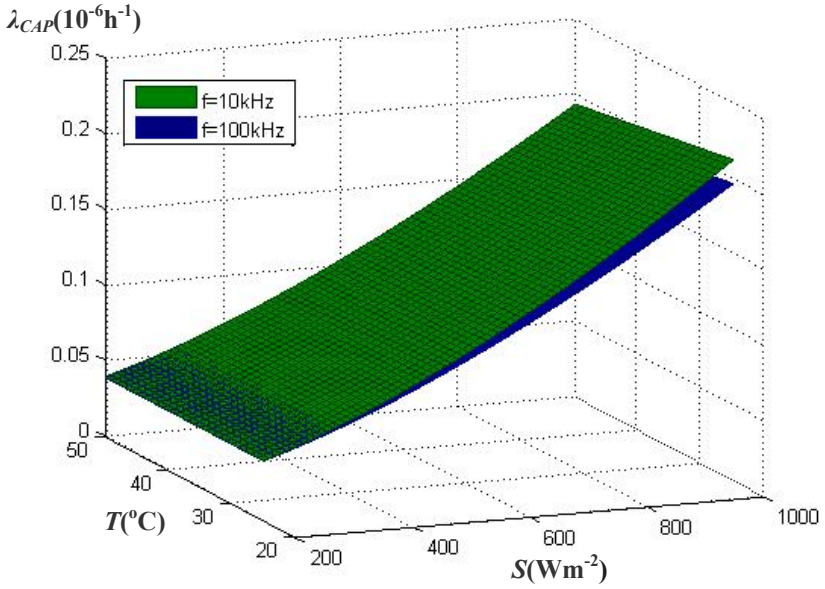


**Figure 26:** Capacitor failure rate as a function of switching frequency

Consider Figures 27 and 28, which demonstrate possible design strategies when picking the number of output capacitors. Figure 27 indicates that four output capacitors, each of them 1.175 μF, enjoy lower failure rates individually as compared to two output capacitors, each of which is 4.7 μF. Figure 28, however, indicates that both options yield the same performance (measured in terms of output voltage ripple) across all possible values of insolation and temperature.

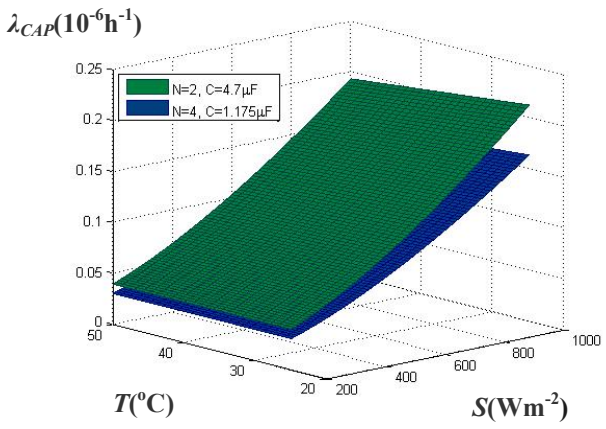


**Figure 27:** $\lambda_{CAP}$ for two possible design choices

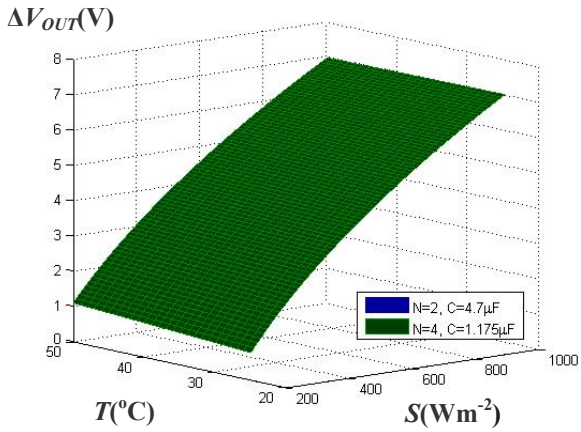


**Figure 28:** $\Delta V_{OUT}$ for the same choices

### 4.2.2 Diode

The impact of number of phases, voltage rating and diode type on diode failure rate, $\lambda_{DIODE}$, is investigated. Figure 29 indicates that definite improvements can be gained by switching to a converter with a higher number of phases. Notice also that $\lambda_{DIODE}$ varies much more with temperature as compared to $\lambda_{CAP}$. In any case, insolation is the more dominant factor and the temperature dependence is more pronounced only at higher values of insolation. Another disparity among $\lambda_{CAP}$ and $\lambda_{DIODE}$ is that for a given value of insolation, $\lambda_{CAP}$ is inversely proportional to temperature, while $\lambda_{DIODE}$ is directly proportional.

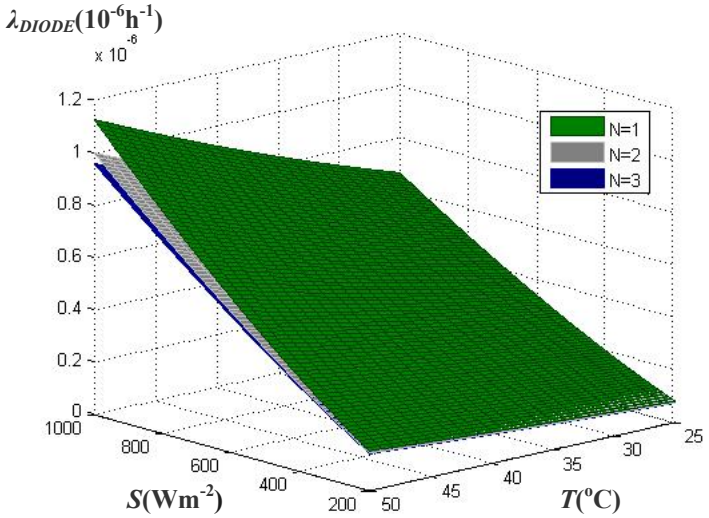


**Figure 29:** Diode failure rate as a function of number of phases

As with the capacitors, the voltage rating of the diodes is of interest. To explore this factor, Figure 30 depicts the variation of $\lambda_{DIODE}$ for a two-phase converter, with the diode voltage ratings varied. A higher voltage rating guarantees lower failure rates across all operating conditions. An interesting observation is that the surface corresponding to the 200 V rating flattens off at low values of insolation and temperature. This is explained by the fact that the stress factor for the diode is constant for voltage stresses below 0.3. Hence, by erudite design, one could pick a voltage rating that would guarantee invariance of the diode failure rate to the output voltage of the converter under all operating conditions. As an example, Figure 31 depicts the diode stress factor, $\pi_S$, for voltage ratings of 150 V and 350 V (which is approximately the maximum output voltage divided by 0.3).

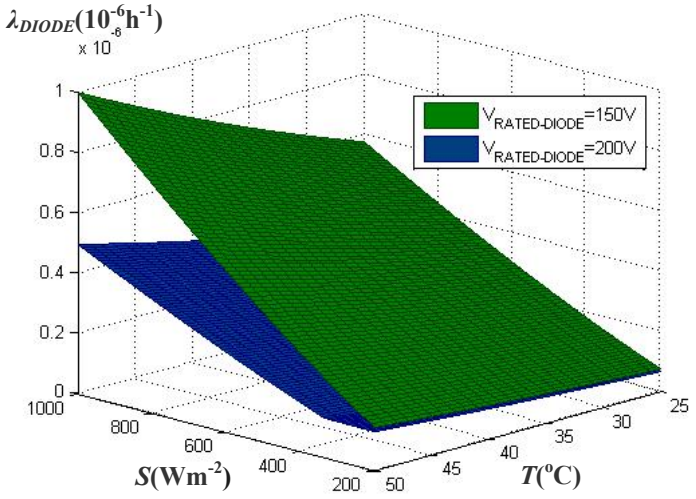


**Figure 30:** Diode failure rate as a function of voltage rating

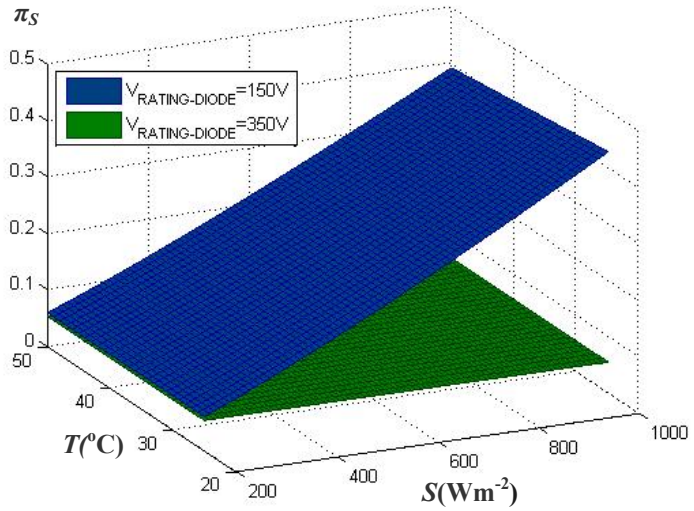


**Figure 31:** Diode stress factor as a function of voltage rating

The justification for employing Schottky diodes is provided illustratively in Figure 32, which demonstrates that Schottky-diode failure rates are an order of magnitude lower than those of fast-recovery power diodes across a wide range of ambient conditions.

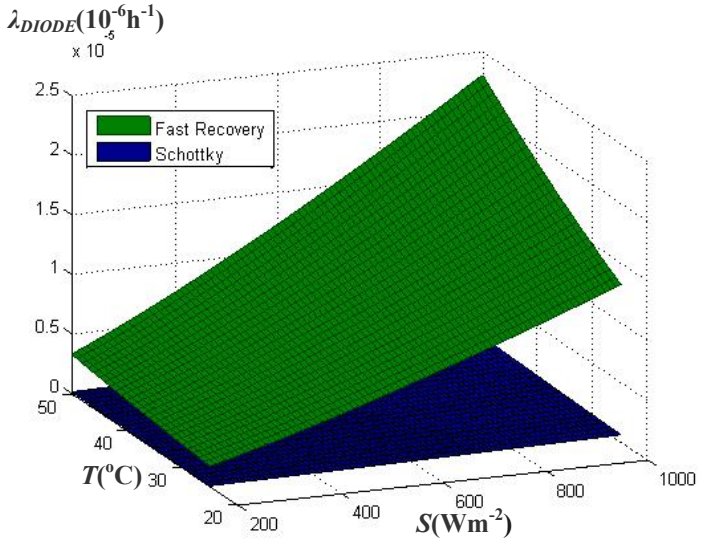


**Figure 32:** Diode failure rate as a function of diode type

### 4.2.3 Active switch

Finally, we consider the failure rates of the field effect transistors, deployed as active switches in the multiphase converter. Figure 33 depicts the variation of the failure rates, $\lambda_{SW}$, for different number of phases, $N$. The temperature dependence of the failure rates is not trifling as was noted with the capacitors. Additionally, there is a directly proportional relationship between $\lambda_{SW}$ and temperature as opposed to the inversely proportional relationship noted between $\lambda_{CAP}$ and temperature.

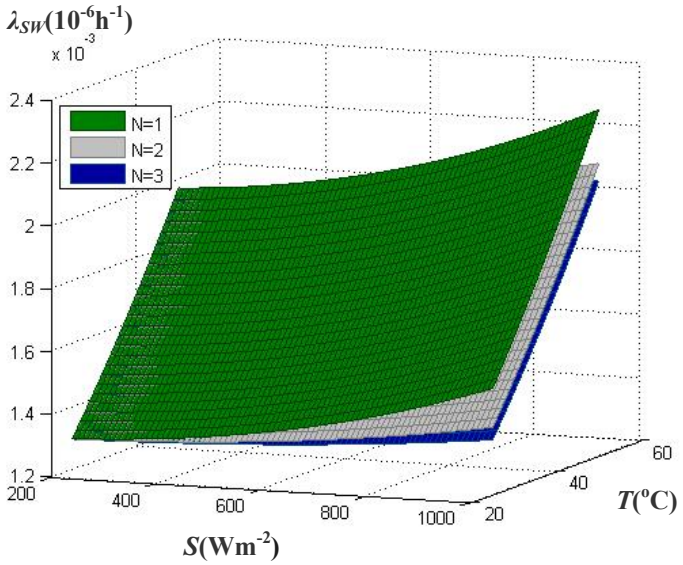


**Figure 33:** Switch failure rate as a function of number of phases

Finally, we inspect the impact of conduction losses on switch reliability. Figure 34 depicts $\lambda_{SW}$ for two disparate values of switch resistance, $r_{SW}$. As expected, a higher switch resistance degrades performance across all possible operating conditions.

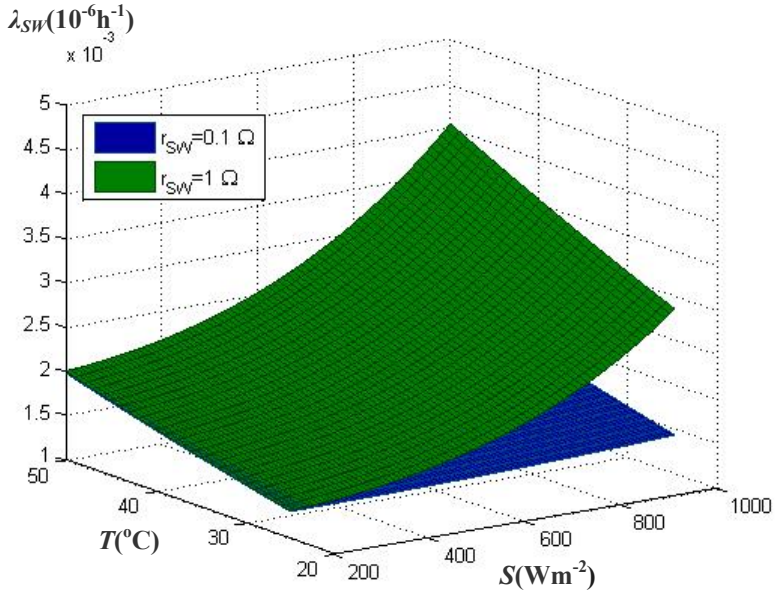


**Figure 34:** Switch failure rate as a function of resistance

# CHAPTER 5

# MARKOV RELIABILITY MODELS

The failure rates in the circuit are noted to be functions of operational conditions, including, but not limited to, number of phases, insolation, temperature, and device ratings. This precludes the possibility of using a combinatorial approach to reliability assessment. Unfortunately, while insolation and temperature vary with time, we cannot effortlessly reflect this in the failure rates. One possible option then is to design for worst-case ambient conditions, while acknowledging the dependence of failure rates on topology. A Markov reliability model serves this method best, as it can incorporate state-dependent failure rates based on converter topologies.

## 5.1 Preliminaries

Before delving into the derivation of the Markov reliability model for the multiphase converter, we present a few definitions and useful concepts below that feature in the forthcoming discussion.

### 5.1.1 Stochastic process

A stochastic process, $X$, is defined as a collection of random variables $\{x(t), t \in T\}$ indexed by a set $T$. The definition is open-ended in terms of the type of set $T$. For the Markov reliability model derived subsequently, the random variables represent possible converter topologies, and the index set is continuous time, ($t \geq 0$).

### 5.1.2 Continuous-time discreet-space Markov process

If the stochastic process, $X$ is indexed by continuous time and the random variables $\{x(t)\}$ assume discrete values in a set $S$, the process is defined as Markovian, if it satisfies the Markov property,

$$\Pr\{x(t_n) = s_n \mid x(t_{n-1}) = s_{n-1}, x(t_{n-2}) = s_{n-2}, .., x(t_0) = s_0\} = \Pr\{x(t_n) = s_n \mid x(t_{n-1}) = s_{n-1}\} \qquad (67)$$

### 5.1.3 Time-homogenous Markov process

Continuous-time, time-homogenous Markovian processes further satisfy the following property:

$$\Pr\{X(t+s)=j \mid X(s)=i\} = \Pr\{X(t)=j \mid X(0)=i\} \forall s,t \geq 0 \tag{68}$$

### 5.1.4 State transition diagram

The Markov reliability model can be graphically represented by the aid of a state-transition diagram. An example for a continuous-time, discrete-space Markov process is illustrated in Figure 35.

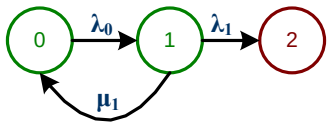


**Figure 35:** Illustrative state-transition diagram

The nodes in the diagram represent the possible states of the Markov process. Each node represents a sample from the discrete space, *S*. For instance, consistent with the notation in (67), state zero represents $x(t) = s_0$, state one represents $x(t) = s_1$ and so on. Some transitions between the states are a consequence of faults that occur with failure rates, $\lambda_i$. The state-transition diagram is augmented by transitions that are illustrative of repairs which restore the operation of failed components (accompanied by repair rates $\mu_i$). States that have no outgoing transitions are indicative of system failure and are referred to as absorbing states (State 2 in Figure 35). Nonabsorbing states are denoted as transient states (States 0 and 1 in Figure 35).

### 5.1.5 Converter operational conditions

The converter can operate in one of many possible states (different from switching topologies analyzed in Chapter 3). Ideally, all phases and output capacitors are functional. However, a generic *N*-phase converter could function with a reduced number of operational phases and a depleted output capacitor bank. The failure of a switch, diode or inductor in each phase would take that phase out of operation, while the capacitor bank could still fulfill its fundamental purpose of energy storage with a single capacitor.

As a matter of notation, we refer to the input stage as that composed of the inductors, switches and diodes, while the output stage refers to the capacitor bank and load. This notation is illustrated in Figure 36.

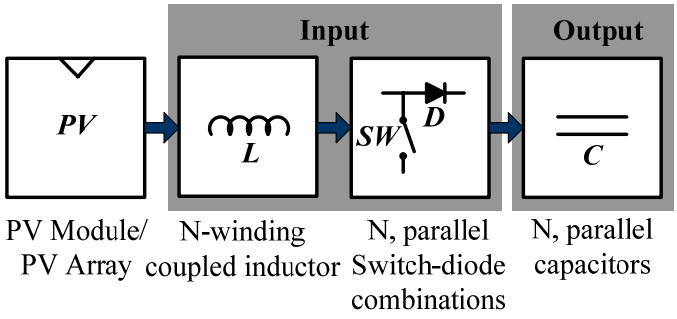


**Figure 36:** Input and output stages highlighted

For instance, a converter with three functional input and output phases is illustrated in Figure 37 and a converter with two functional input phases and three functional output phases is illustrated in Figure 38. The state-space description for the Markov model is increasingly complicated due to the large number of operational possibilities. Consider two possible topologies that emanate due to component failures in a three-phase converter. Configuration 1 (Figure 37) results from a failure in one of the output capacitors, while configuration 2 (Figure 38) results from a failure in the inductors, switches or diodes in the original three-phase converter. From the formulation of the failure rates of the different devices, it emerges that the stress imposed on the input stage is a function of the number of input phases and independent of the number of output capacitors. This is, however, untrue for the capacitor bank. In general, the voltage stress on the capacitors is a function of both the number of functional input phases and the number of functional capacitors in the bank.

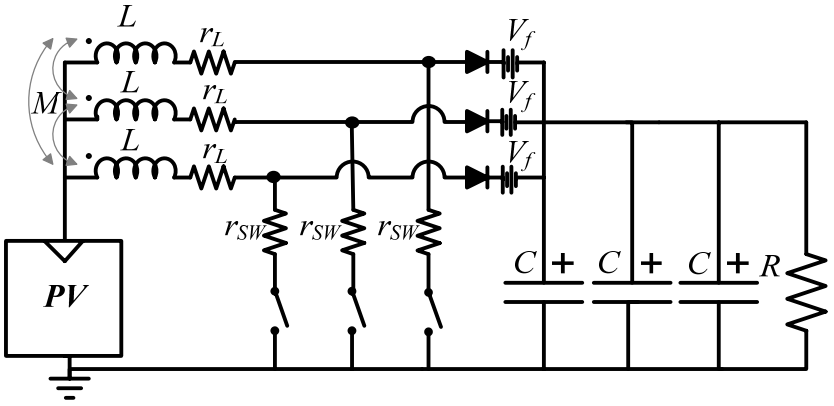


**Figure 37:** Configuration 1 – All stages operational

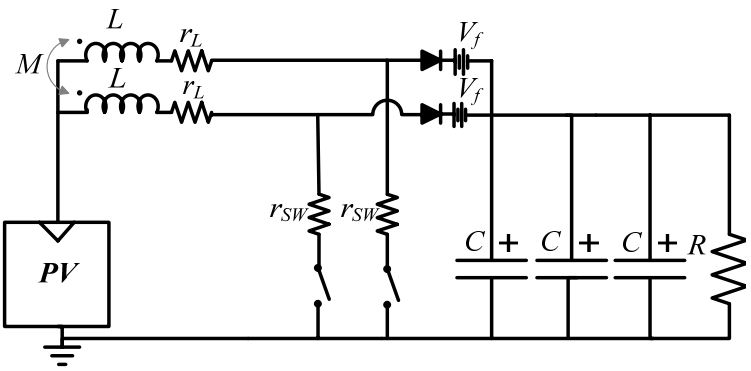


**Figure 38:** Configuration 2 – Two input stages and three output stages functional

To appreciate why the capacitors experience different levels of stress based on the number of input phases, consider the expressions for the output voltage and output voltage ripple repeated below:

$$V_{OUT} = IR(1 - D_{SW}N) \tag{69}$$

$$\Delta V_{OUT} = \left( I - \frac{V_{OUT}}{R} \right) \frac{D_D}{fN_C C} \tag{70}$$

For a given load, the average output voltage is independent of the number of functional input phases or the number of functional output capacitors. This is illustrated by Figure 39, which plots the function, $f(D_{SW},N) = 1 - D_{SW}N$, versus insolation and ambient temperature for different values of $N$ (converter specifications same as those attached in Table 4).

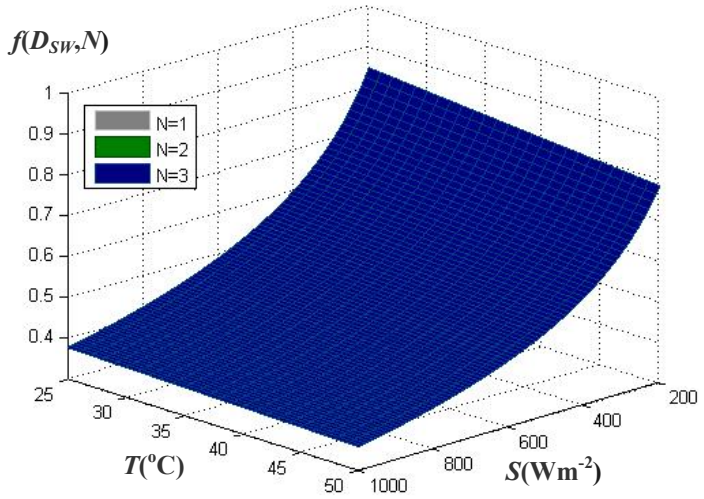


**Figure 39:** The function $f(D_{SW},N)$ for different values of $N$

On the other hand, the output voltage ripple is a function of the duty ratio of the active switch, $D_{SW}$, and the number of output capacitors, $N_C$. Hence, the ripple experienced by a capacitor in a converter with, say, two input and three output phases would be different from that experienced with three input and three output phases. This is illustrated in Figure 40.

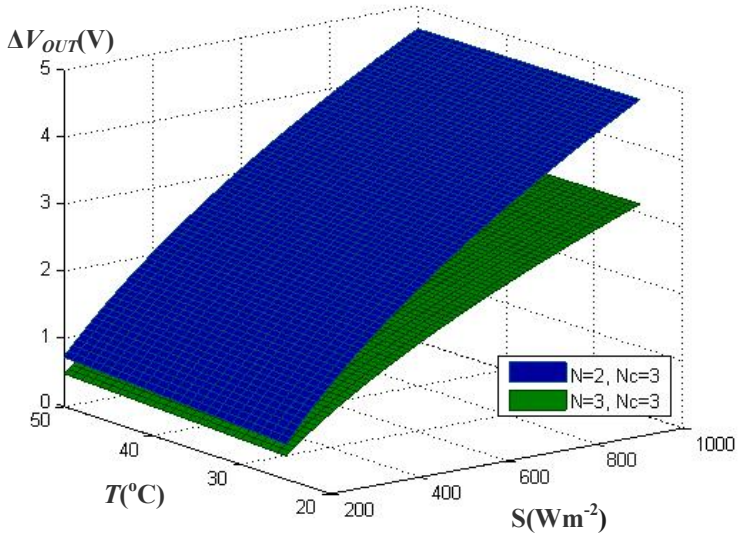


**Figure 40:** Output voltage ripple for different number of input and output stages

## 5.2 State-Transition Diagrams for Three-Phase and Two-Phase Converters

The derivation of the state-transition diagram for a generic $N$-phase converter will be illustrated in the context of three-phase and two-phase examples. Repairs are neglected and all failure rates are constant, adapted from [47] and of the form presented in (45). Each possible topology of the converter is a state of the Markov process. For the three-phase converter, the following states are possible:

a. State 00: Completely operational
b. State 10: one input phase failed, no output capacitors failed
c. State 20: two input phases failed, no output capacitors failed
d. State 01: no input phases failed, one output capacitor failed
e. State 02: no input phases failed, two output capacitors failed
f. State 11: one input phase failed, one output capacitor failed
g. State 12: one input phase failed, two output capacitors failed
h. State 21: two input phases failed, one output capacitor failed
i. State 22: two input phases failed, two output capacitors failed
j. State 33: Converter not operational

A total of 9 (=$3^2$) operational and 1 failed states are noted. In general, for an $N$-phase converter, a total of $N^2 + 1$ states can be envisioned.

The failure rate of the switches and diodes in the converter are represented as $\lambda_{SWx}$ and $\lambda_{Dx}$ (respectively), $0 \le x \le 2$, where $x$ represents the number of failed input phases. The failure rates of the capacitors in the output stage are of the form $\lambda_{CAPxy}$, $0 \le x \le 2$, $0 \le y \le 2$. The first index represents the number of failed input stages and the second represents the number of failed output capacitors. Note that the failure rates of the switching devices are independent of the number of output capacitors, while the same is not true for the capacitors. This is consistent with the discussion earlier.

The state-transition diagram in Figure 41 follows based on the discussion thus far. Notice that transitions to the failed state only occur from the nodes at the edge of the diagram. The multiplicative factors for pertinent failure rates will be explained on a subsequent section on aggregation.

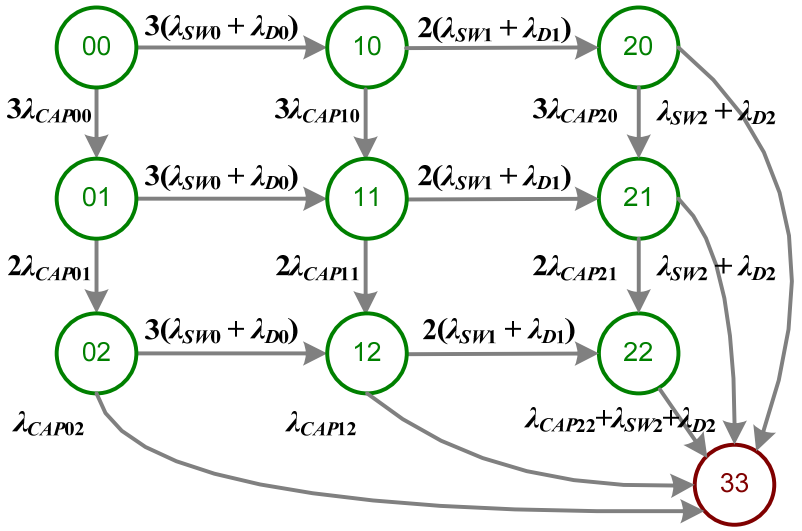


**Figure 41:** State transition diagram – Three-phase converter

Along similar lines, the state-transition diagram for a two-phase converter can be determined. To begin, we list the possible topologies in which the converter can operate:

a. State 00: Completely operational

b. State 10: one input phase failed, no output capacitors failed

c. State 01: no input phases failed, one output capacitor failed

d. State 11: one input phase failed, one output capacitor failed

e. State 22: Converter not operational

Based on the documentation of the possible topological states, the state-transition diagram in Figure 42 can be drafted.

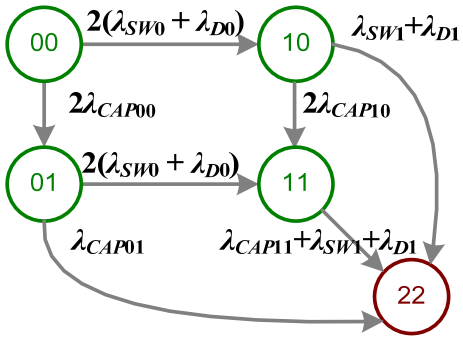


**Figure 42:** State-transition diagram – Two-phase converter

### 5.2.1 Aggregation

It is worthwhile to examine the choice of failure rates for the various transitions in the state-transition diagram. For instance, with reference to the three-phase converter, the state corresponding to two operational input phases and three operational output phases is considered. The topology in question is depicted in Figure 43, while the relevant portion of the state-transition diagram with outgoing transitions is depicted in Figure 44. The reliability block diagrams pertaining to failures in input and output phases are depicted in Figures 45 and 46, respectively.

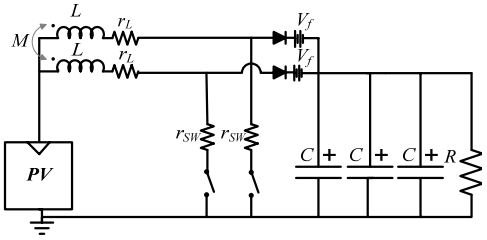


**Figure 43:** Topology corresponding to State 10

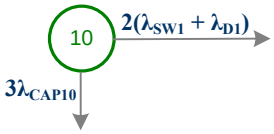


**Figure 44:** Transitions out of State 10

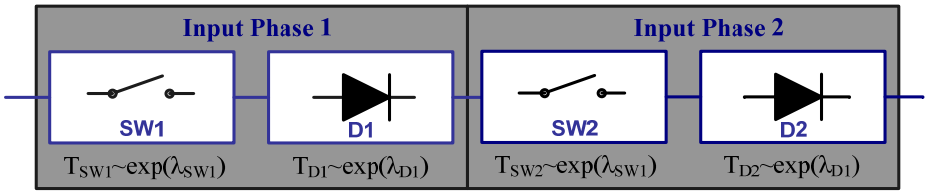


**Figure 45:** Reliability block diagram – Input phases

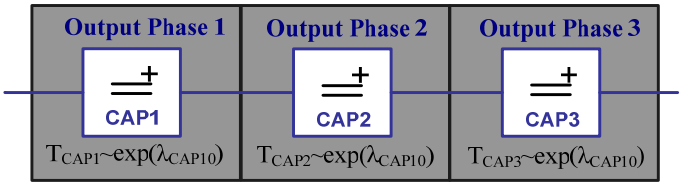


**Figure 46:** Reliability block diagram – Output phases

The failure of any component in the topology coerces the Markov process to transition to another state, hence justifying the rationale for connecting the components in series in the reliability block diagrams. Since all components in a particular phase (input / output) experience the same stress, they have the same failure rates.

We assume that the failure of the components is independent and determined by exponential probability distribution functions owing to the time-invariant character of the failure rates. The failure rate of the input stage will be derived, and since the output stage has a similarly structured reliability block diagram (series connection), the failure rate of the output stage follows by inspection.

Define random variables, $T_{SW1}$, $T_{D1}$, $T_{SW2}$ and $T_{D2}$ to denote the time to failure of the switches and diodes in the input stage. In addition, denote, $T_{INPUT}$ as the random variable that captures the time to failure of the input stage. From the definition of the reliability function presented in (46), the reliability of the input stage can be expressed as

$$R_{INPUT}(t) = \Pr\{T_{INPUT} > t\} \tag{71}$$

With reference to the reliability block diagram in Figure 45,

$$R_{INPUT}(t) = \Pr\{T_{SW1} > t \cap T_{SW2} > t \cap T_{D1} > t \cap T_{D2} > t\} \tag{72}$$

Given the assumption of independence of failures and employing the reliability function formulation for constant failure rates prescribed in (52),

$$\begin{aligned} R_{INPUT}(t) &= \Pr\{T_{SW1} > t\} \Pr\{T_{SW2} > t\} \Pr\{T_{D1} > t\} \Pr\{T_{D2} > t\} \\ &= \exp(-\lambda_{SW1} t) \exp(-\lambda_{SW1} t) \exp(-\lambda_{D1} t) \exp(-\lambda_{D1} t) \\ &= \exp[-2(\lambda_{SW} + \lambda_{D})t] \end{aligned} \tag{73}$$

This suggests that the random variable, $T_{INPUT}$, that captures the reliability of the input phase is exponentially distributed with failure rate $2(\lambda_{SW1} + \lambda_{D1})$, hence justifying the representation in the state transition diagram (Figure 44).

Similarly, we can prove that the reliability of the output phase can be captured by an exponential probability distribution function with failure rate $3\lambda_{CAP10}$.

### 5.2.2 Chapman – Kolmogorov equations

Consider a Markov process that resides in state $i$ at time $t$. That is, $x(t) = i$. The period of time the process spends in this state can be described by a random variable $T_i$. Given the Markovian nature of the process, the probability that the process remains in state $i$ at time $t+\Delta t$ simplifies to

$$\Pr\{T_i > t + \Delta t \mid T_i > \Delta t\} = \Pr\{T_i > t\} \tag{74}$$

The Markov property hence renders the random variable $T_i$ memoryless, and for the sake of notation it can be established that $T_i$ is exponentially distributed with parameter $\eta_i$. The rate at which the Markov process makes a transition from stage $i$ to $j$, $\lambda_{ij}$, can be described based on the parameter $\eta_i$ and the probability of transition $P_{ij}$ as

$$\lambda_{ij} = \eta_i P_{ij} \tag{75}$$

The probabilities of transition between different states can be grouped collectively in a matrix:

$$\mathbf{P}(t) = \begin{bmatrix} P_{00}(t) & P_{01}(t) & .. & P_{0N}(t) \\ P_{10}(t) & P_{11}(t) & .. & P_{1N}(t) \\ .. & .. & P_{ij}(t) & .. \\ P_{N0}(t) & P_{N1}(t) & .. & P_{NN}(t) \end{bmatrix} \tag{76}$$

Note that each row in the probability transition matrix must sum to one:

$$\sum_{\substack{j=0 \\ j \neq i}}^{N} P_{ij} = 1 \; ; \; \forall \quad 0 \leq i \leq N \tag{77}$$

From the definition of the transition rate, $\lambda_{ij}$, in (75) and the observation in (77),

$$\sum_{\substack{j=1 \\ j \neq i}}^{N} \lambda_{ij} = \eta_i \sum_{\substack{j=1 \\ j \neq i}}^{N} P_{ij} \tag{78}$$

For the case $i = j$, define:

$$\lambda_{ii} = -\eta_i = -\sum_{\substack{j=1 \\ j \neq i}}^{N} \lambda_{ij} \tag{79}$$

The transition rates can be grouped collectively to form the State-transition matrix:

$$\mathbf{\Lambda} = \begin{bmatrix} \lambda_{00} & \lambda_{01} & .. & \lambda_{0N} \\ \lambda_{10} & \lambda_{11} & .. & \lambda_{1N} \\ .. & .. & \lambda_{ij} & .. \\ \lambda_{N0} & \lambda_{N1} & .. & \lambda_{NN} \end{bmatrix} \tag{80}$$

With reference to the state-transition diagrams shown earlier, note that $\lambda_{ij}$ represents the failure rate that causes a transition from state $i$ to $j$.

The Kolmogorov forward equations describe the time evolution of the transition probabilities considered above. Their derivation follows from the well known Chapman-Kolmogorov equations [47]. The results indicate that the transition probabilities conform to the following differential equation:

$$\frac{dP_{ij}(t)}{dt} = \sum_{k=0}^{N} \lambda_{kj} P_{ik}(t) \tag{81}$$

Assuming that the Markov process resides in some state *i* at time 0, the notation can be further simplified by expressing $P_{ij}(t)$ as $P_j(t)$. Thus, the distribution of the Markov process at any time *t* can be simply expressed by the state vector,

$$\mathbf{P}(t) = [P_0(t) \quad P_1(t) \quad .. \quad P_N(t)] \tag{82}$$

Congruently, the Kolmogorov forward equations can be rewritten as

$$\frac{dP_j(t)}{dt} = \sum_{k=0}^{N} \lambda_{kj} P_k(t) \tag{83}$$

Using the state-transition matrix, this can be expressed in matrix form as

$$[\frac{dP_0(t)}{dt} \quad \frac{dP_1(t)}{dt} \quad .. \quad \frac{dP_N(t)}{dt}] = [P_0(t) \quad P_1(t) \quad .. \quad P_N(t)] \begin{bmatrix} \lambda_{00} & \lambda_{01} & .. & \lambda_{0N} \\ \lambda_{10} & \lambda_{11} & .. & \lambda_{1N} \\ .. & .. & \lambda_{ij} & .. \\ \lambda_{N0} & \lambda_{N1} & .. & \lambda_{NN} \end{bmatrix} \tag{84}$$

with the additional constraint and initial condition:

$$\sum_{j=0}^{N} P_j(t) = 1 \tag{85}$$

$$P_i(0) = 1 \tag{86}$$

The definition of the diagonal entries of the state-transition matrix indicates that it is singular. Hence, (85) and (86) are required to obtain a solution to (84). Equation (85) suggests the obvious in that the Markov process resides in *some* state at time *t*, while (86) specifies that the process begins in state *i* at time 0.

### 5.2.3 Absorbing states

From the state-transition diagrams presented in Figures 41 and 42 (pages 43 and 44, respectively) we note that the reliability model includes an absorbing state. Since there are no transitions out of the absorbing state, the entries in the last row of the state-transition matrix are all identically zero. Effectively, the last row of the state-transition matrix and the last element of $\mathbf{P}(t)$, $P_N(t)$, can be discarded. While the summation in (85) and the initial condition in (86) still apply, (84) simplifies to a reduced set of equations,

$$[\frac{dP_0(t)}{dt} \quad \frac{dP_1(t)}{dt} \quad .. \quad \frac{dP_{N-1}(t)}{dt}] = [P_0(t) \quad P_1(t) \quad .. \quad P_{N-1}(t)] \begin{bmatrix} \lambda_{00} & \lambda_{01} & .. & \lambda_{0N} \\ \lambda_{10} & \lambda_{11} & .. & \lambda_{1N} \\ .. & .. & \lambda_{ij} & .. \\ \lambda_{(N-1)0} & \lambda_{(N-1)1} & .. & \lambda_{(N-1)(N-1)} \end{bmatrix} \tag{87}$$

Denoting the reduced probability vector as $\mathbf{P_R}(t)$ and the reduced state-transition matrix as $\mathbf{\Lambda_R}$, we can rewrite (84) as

$$\frac{d\mathbf{P_R}(t)}{dt} = \mathbf{P_R}(t)\mathbf{\Lambda_R} \tag{88}$$

The solution to (88) can be greatly simplified by employing the Laplace transform. To that end, define the Laplace variable as $s$ and recall that the Laplace transform of a continuous-time function $X(t)$ can be expressed as

$$X^*(s) = \int_{t=0}^{\infty} X(t)\exp(-st)dt \tag{89}$$

Taking the Laplace transform of both sides in (88) in accordance with the initial condition in (86) allows us to solve for $\mathbf{P_R}^*(s)$. The inverse Laplace transform then yields the elements of the reduced transition-probability vector.

## 5.3 Metrics to Quantify System Reliability and Performance

We now present the background to some of the metrics used to acknowledge the performance and reliability of the converter.

### 5.3.1 Mean time to system failure

The mean time to system failure, *MTTF*, is defined as

$$MTTF = \int_{t=0}^{\infty} R(t)dt \tag{90}$$

In the above expression, $R(t)$ denotes the reliability function of the system. From the discussion presented thus far, note that the reliability function could be expressed as the sum of the elements of the reduced transition-probability vector,

$$R(t) = \sum_{i=0}^{N-1} \mathbf{P}_{\mathbf{R}i}(t) \tag{91}$$

Taking the Laplace transform of both sides in (91) yields

$$R^*(s) = \sum_{i=0}^{N-1} \mathbf{P}_{\mathbf{R}i}{}^*(s) \tag{92}$$

Employing the definition in (89), the Laplace transform of the reliability function, $R^*(s)$, can be expressed as

$$R^*(s) = \int_{t=0}^{\infty} R(t)\exp(-st)dt \tag{93}$$

The *MTTF* can hence be determined as

$$MTTF = \int_{t=0}^{\infty} R(t)dt = \int_{t=0}^{\infty} R(t)\exp(-0t)dt = R^*(0) \tag{94}$$

In essence, (94) suggests that the MTTF can be found simply from the Laplace transform of the reliability function.

### 5.3.2 Expected energy loss

Owing to the memoryless property of Markov chains, the time spent in a given state is an exponentially distributed random variable. The corresponding failure rate is the sum of all device failure rates that accompany transitions out of the state. For instance, consider the section of the Markov reliability model for the three-phase converter depicted in Figure 44. For convenience, it is redrawn in Figure 47.

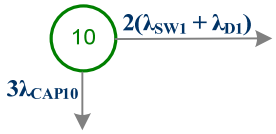


**Figure 47:** Transitions out of State 10

Denote the time spent in State 10 by the random variable, $T_{10}$. The expected value of $T_{10}$ is defined as the mean sojourn time (in state 10) and is an estimate of the average duration of time spent in the state:

$$E[T_{10}] = \frac{1}{3\lambda_{CAP10} + 2(\lambda_{SW1} + \lambda_{D1})} \tag{95}$$

This expectation can be promptly estimated from the relevant diagonal term of the state-transition diagram. In general, with reference to the state-transition matrix proposed in (80) the expected value of $T_j$, the average duration of time spent in state $j$, is given by

$$E[T_j] = \frac{1}{\lambda_{jj}} \tag{96}$$

The power losses in the converter are a function of the state in which the Markov process resides, as each state corresponds to a particular topology. Recall from earlier that the converter model includes conduction losses in the switches, $P_{SW}$, losses due to forward voltage drops in the diodes, $P_D$, and conduction losses in the coupled inductor, $P_L$.

From the steady-state characterization of the converter, we note that the above losses can be quantized as

$$P_{SW} = NI^2 r_{SW} D_{SW} \tag{97}$$

$$P_D = NIV_f D_D \tag{98}$$

$$P_L = NI^2 r_L \tag{99}$$

For any given state *j* in the Markov reliability model, define the total power loss as the sum of the above losses:

$$P_{LOSS-j} = P_{SW-j} + P_{D-j} + P_{L-j} \tag{100}$$

Based on these preliminaries, we define the expected energy loss in a given state of the Markov process as the product of the total power losses in the state and the average duration of time spent in the state. Based on the discussion of PV-system performance presented in Chapter 1, a capacity factor is introduced to provide a better estimate. This in fact forces a geographic dependence on the expected energy loss. Recall that the capacity factor is the ratio of the hours per day of peak-sun to the number of hours in a day. Denoting the expected energy loss as *EEL* and the capacity factor as *CF*,

$$EEL = CF\sum_{j=0}^{N-1} E[T_j]P_{LOSS-j} = CF\sum_{j=0}^{N-1} \frac{P_{LOSS-j}}{\lambda_{jj}} \tag{101}$$

### 5.3.3 Expected system efficiency

To normalize the expected energy loss metric, we introduce the Expected Energy Efficiency (*ESE*). To compute the *ESE*, we first estimate the energy sourced by the PV module, denoted as *EPV*, and defined as

$$EPV = (CF)(P)\sum_{j=0}^{N-1} E[T_j] = (CF)(P)\sum_{j=0}^{N-1} \frac{1}{\lambda_{jj}} \tag{102}$$

In the above expression, *P* denotes the rated power available from the PV module under STC. The *ESE* is then expressed as

$$ESE = 1 - \frac{EEL}{EPV} \tag{103}$$

Substituting (101) and (102) in (103),

$$ESE = 1 - \frac{\sum_{j=0}^{N-1} \frac{P_{LOSS-j}}{\lambda_{jj}}}{(P)\sum_{j=0}^{N-1} \frac{1}{\lambda_{jj}}} \tag{104}$$

The formulation suggests that the Expected Energy Output (*EEO*) of the multiphase converter can be expressed as:

$$EEO = CF \sum_{j=0}^{N-1} \frac{(P - P_{LOSS-j})}{\lambda_{jj}} \tag{105}$$

## 5.4 Case Studies

The Kolmogorov forward equations will be solved for three-phase and two-phase converters. Relevant reliability metrics presented earlier are then evaluated to assess the impact of converter design on reliability.

### 5.4.1 Three-phase converter

The Kolmogorov forward equations for the three-phase converter (state-transition diagram in Figure 41) can be written simply as

$$\frac{d\mathbf{P}(t)}{dt} = \mathbf{P}\boldsymbol{\Lambda} \tag{106}$$

where

$$\mathbf{P} = [P_{00}(t) \quad P_{01}(t) \quad P_{02}(t) \quad P_{10}(t) \quad P_{11}(t) \quad P_{12}(t) \quad P_{20}(t) \quad P_{21}(t) \quad P_{22}(t) \quad P_{33}(t)] \tag{107}$$

$$\boldsymbol{\Lambda} = \begin{bmatrix} -3(\lambda_{CAP00}+\lambda_{SW0}+\lambda_{D0}) & 3\lambda_{CAP00} & 0 & 3(\lambda_{SW0}+\lambda_{D0}) \\ 0 & -2\lambda_{CAP01}-3(\lambda_{SW0}+\lambda_{D0}) & 2\lambda_{CAP01} & 0 \\ 0 & 0 & -\lambda_{CAP02}-3(\lambda_{SW0}+\lambda_{D0}) & 0 \\ 0 & 0 & 0 & -3\lambda_{CAP10}-2(\lambda_{SW1}+\lambda_{D1}) \\ 0 & 0 & 0 & 0 \\ 0 & 0 & 0 & 0 \\ 0 & 0 & 0 & 0 \\ 0 & 0 & 0 & 0 \\ 0 & 0 & 0 & 0 \\ 0 & 0 & 0 & 0 \end{bmatrix} \cdots$$

$$\cdots \begin{bmatrix} 0 & 0 & 0 & 0 \\ 3(\lambda_{SW0}+\lambda_{D0}) & 0 & 0 & 0 \\ 0 & 3(\lambda_{SW0}+\lambda_{D0}) & 0 & 0 \\ 2\lambda_{CAP10} & 0 & 2(\lambda_{SW1}+\lambda_{D1}) & 0 \\ -2\lambda_{CAP11}-2(\lambda_{SW1}+\lambda_{D1}) & 2\lambda_{CAP11} & 0 & 2(\lambda_{SW1}+\lambda_{D1}) \\ 0 & -\lambda_{CAP12}-2(\lambda_{SW1}+\lambda_{D1}) & 0 & 0 \\ 0 & 0 & -3\lambda_{CAP20}-\lambda_{SW2}-\lambda_{D2} & 3\lambda_{CAP20} \\ 0 & 0 & 0 & -2\lambda_{CAP21}-\lambda_{SW2}-\lambda_{D2} \\ 0 & 0 & 0 & 0 \\ 0 & 0 & 0 & 0 \end{bmatrix} \cdots$$

$$\cdots \begin{bmatrix} 0 & 0 \\ 0 & 0 \\ 0 & \lambda_{CAP02} \\ 0 & 0 \\ 0 & 0 \\ 2(\lambda_{SW1}+\lambda_{D1}) & \lambda_{CAP02} \\ 0 & \lambda_{SW2}+\lambda_{D2} \\ 2\lambda_{CAP21} & \lambda_{SW2}+\lambda_{D2} \\ -\lambda_{SW2}-\lambda_{D2}-\lambda_{CAP22} & \lambda_{SW2}+\lambda_{D2}+\lambda_{CAP22} \\ 0 & 0 \end{bmatrix} \tag{108}$$

The following initial-condition vector presumes the converter is fully functional at time, $t = 0$:

$$\mathbf{P}(0) = [1 \quad 0 \quad 0 \quad 0 \quad 0 \quad 0 \quad 0 \quad 0 \quad 0 \quad 0] \tag{109}$$

Contingent to the discussion presented earlier, a reduced-order state space is considered,

$$\frac{d\mathbf{P_R}(t)}{dt} = \mathbf{P_R}\mathbf{\Lambda_R} \tag{110}$$

where $\mathbf{\Lambda_R}$ is the same as (108) sans the last row, and $\mathbf{P_R}(t)$ is defined as

$$\mathbf{P_R}(t) = [P_{00}(t) \quad P_{01}(t) \quad P_{02}(t) \quad P_{10}(t) \quad P_{11}(t) \quad P_{12}(t) \quad P_{20}(t) \quad P_{21}(t) \quad P_{22}(t) \quad ] \tag{111}$$

The initial-condition vector follows analogously to (109) with a reduced number of elements,

$$\mathbf{P_R}(0) = [1 \quad 0 \quad 0 \quad 0 \quad 0 \quad 0 \quad 0 \quad 0 \quad 0 \quad ] \tag{112}$$

Taking the Laplace transform of both sides in (110) yields the following linear equations:

$$-3(\lambda_{CAP00} + \lambda_{SW0} + \lambda_{D0})P_{00}^*(s) = sP_{00}^*(s) - 1 \tag{113}$$

$$3\lambda_{CAP00}P_{00}^*(s) + [-2\lambda_{CAP01} - 3(\lambda_{SW0} + \lambda_{D0})]P_{01}^*(s) = sP_{01}^*(s) \tag{114}$$

$$2\lambda_{CAP01}P_{01}^*(s) + [-\lambda_{CAP02} - 3(\lambda_{SW0} + \lambda_{D0})]P_{02}^*(s) = sP_{02}^*(s) \tag{115}$$

$$3(\lambda_{SW0} + \lambda_{D0})P_{00}^*(s) + [-3\lambda_{CAP10} - 2(\lambda_{SW1} + \lambda_{D1})]P_{10}^*(s) = sP_{10}^*(s) \tag{116}$$

$$3(\lambda_{SW0} + \lambda_{D0})P_{01}^*(s) + (3\lambda_{CAP10})P_{10}^*(s) + [-2\lambda_{CAP11} - 2(\lambda_{SW1} + \lambda_{D1})]P_{11}^*(s) = sP_{11}^*(s) \tag{117}$$

$$3(\lambda_{SW0} + \lambda_{D0})P_{02}^*(s) + (2\lambda_{CAP11})P_{11}^*(s) + [-\lambda_{CAP12} - 2(\lambda_{SW1} + \lambda_{D1})]P_{12}^*(s) = sP_{12}^*(s) \tag{118}$$

$$2(\lambda_{SW1} + \lambda_{D1})P_{10}^*(s) + [-3\lambda_{CAP20} - \lambda_{SW2} - \lambda_{D2}]P_{20}^*(s) = sP_{20}^*(s) \tag{119}$$

$$2(\lambda_{SW1} + \lambda_{D1})P_{11}^*(s) + (3\lambda_{CAP20})P_{20}^*(s) + [-2\lambda_{CAP21} - \lambda_{SW2} - \lambda_{D2}]P_{21}^*(s) = sP_{21}^*(s) \tag{120}$$

$$2(\lambda_{SW1} + \lambda_{D1})P_{12}^*(s) + (2\lambda_{CAP21})P_{21}^*(s) + [-\lambda_{SW2} - \lambda_{D2} - \lambda_{CAP22}]P_{22}^*(s) = sP_{22}^*(s) \tag{121}$$

Equations (113)-(121) are solved for the transition probabilities:

$$P_{00}^*(s) = \frac{1}{s + 3(\lambda_{CAP00} + \lambda_{SW0} + \lambda_{D0})} \tag{122}$$

$$P_{01}^*(s) = \frac{3\lambda_{CAP00}}{[s + 2\lambda_{CAP01} + 3(\lambda_{SW0} + \lambda_{D0})]}P_{00}^*(s) \tag{123}$$

$$P_{02}^*(s) = \frac{2\lambda_{CAP01}}{[s + \lambda_{CAP02} + 3(\lambda_{SW0} + \lambda_{D0})]}P_{01}^*(s) \tag{124}$$

$$P_{10}^{*}(s) = \frac{3(\lambda_{SW0} + \lambda_{D0})}{[s + 3\lambda_{CAP10} + 2(\lambda_{SW1} + \lambda_{D1})]} P_{00}^{*}(s) \tag{125}$$

$$P_{11}^{*}(s) = \frac{3(\lambda_{SW0} + \lambda_{D0})}{[s + 2\lambda_{CAP11} + 2(\lambda_{SW1} + \lambda_{D1})]} P_{01}^{*}(s) + \frac{(3\lambda_{CAP10})}{[s + 2\lambda_{CAP11} + 2(\lambda_{SW1} + \lambda_{D1})]} P_{10}^{*}(s) \tag{126}$$

$$P_{12}^{*}(s) = \frac{3(\lambda_{SW0} + \lambda_{D0})}{[s + \lambda_{CAP12} + 2(\lambda_{SW1} + \lambda_{D1})]} P_{02}^{*}(s) + \frac{(2\lambda_{CAP11})}{[s + \lambda_{CAP12} + 2(\lambda_{SW1} + \lambda_{D1})]} P_{11}^{*}(s) \tag{127}$$

$$P_{20}^{*}(s) = \frac{2(\lambda_{SW1} + \lambda_{D1})}{[s + 3\lambda_{CAP20} + \lambda_{SW2} + \lambda_{D2}]} P_{10}^{*}(s) \tag{128}$$

$$P_{21}^{*}(s) = \frac{2(\lambda_{SW1} + \lambda_{D1})}{[s + 2\lambda_{CAP21} + \lambda_{SW2} + \lambda_{D2}]} P_{11}^{*}(s) + \frac{(3\lambda_{CAP20})}{[s + 2\lambda_{CAP21} + \lambda_{SW2} + \lambda_{D2}]} P_{20}^{*}(s) \tag{129}$$

$$P_{22}^{*}(s) = \frac{2(\lambda_{SW1} + \lambda_{D1})}{[s + \lambda_{SW2} + \lambda_{D2} + \lambda_{CAP22}]} P_{12}^{*}(s) + \frac{(2\lambda_{CAP21})}{[s + \lambda_{SW2} + \lambda_{D2} + \lambda_{CAP22}]} P_{21}^{*}(s) \tag{130}$$

To compute the *MTTF* of the converter, we employ the definition of the Laplace transform of the reliability function presented in (92) and the ensuing equation in (94)

$$R^{*}(s) = P_{00}^{*}(s) + P_{01}^{*}(s) + P_{02}^{*}(s) + P_{10}^{*}(s) + P_{11}^{*}(s) + P_{12}^{*}(s) + P_{20}^{*}(s) + P_{21}^{*}(s) + P_{22}^{*}(s) \tag{131}$$

$$MTTF = R^{*}(0) = P_{00}^{*}(0) + P_{01}^{*}(0) + P_{02}^{*}(0) + P_{10}^{*}(0) + P_{11}^{*}(0) + P_{12}^{*}(0) + P_{20}^{*}(0) + P_{21}^{*}(0) + P_{22}^{*}(0) \tag{132}$$

The studies presented in Chapter 4 indicate that the failure rates are a function of the incident insolation, ambient temperature, and number of phases. Employing a Markov reliability model for analysis allows us to circumvent the last impediment, but does not acknowledge the impact of ambient conditions on the failure rates. In particular, the homogeneity assumption in the definition of the Markovian process naturally lends itself to time-invariant failure rates, which are in fact adapted to characterize the components in the converter. Hence the reliability of the converter is estimated under worst-case ambient conditions. The design temperature is pessimistic at best and realistic at worst.

- Location – Los Angeles, CA (solar radiation data given in Table 2).
- Incident Insolation, $S = 1000$ W/m$^2$
- Ambient Temperature, $T_{AMB} = 21.3$ $^{o}$C
- Design Temperature, $T = 85$ $^{o}$C
- Rating of PV module, $P = 230$ W

Six different case studies are performed to assess the dominant factors that affect the reliability of the three-phase converter, and the results are tabulated in Table 8. Reducing the voltage rating of the output capacitors drastically reduces the *MTTF* of the converter. Notice, however, that reducing the voltage rating of the diodes does not change the *MTTF* from the base case. While it might be imagined that using higher capacitance would reduce stress by decreasing the output-voltage ripple, the capacitance factor (57) significantly impacts the failure of the output capacitors, indicative of the reduced *MTTF* in case four. Finally, the most startling result emerges from cases 5 and 6. Increasing the resistance of the active switches and the forward voltage drops of the diodes is seen to increase the reliability of the converter. This is because, as the switches become lossier, the output voltage decreases, thereby reducing the voltage stress on the output capacitor bank. Since the reliability of the converter is determined predominantly by the output capacitors, it turns out that a converter design with inferior switches has a longer mean time to failure.

TABLE 8
*MTTF*, *EEL*, *ESE* – THREE PHASE CONVERTER

| Case Study | Component Specifications | | MTTF (YEARS) | EEL (MW-s) | ESE (%) |
|---|---|---|---|---|---|
| 1 Base Case | $V_{RATED\text{-}CAP}$ | 100 V | 944 | 58.57 | 95.12 |
| | $V_{RATED\text{-}DIODE}$ | 150 V | | | |
| | $r_{SW}$ | 0.1 Ω | | | |
| | $C$ | 4.7 µF | | | |
| | $V_f$ | 1 V | | | |
| 2 $V_{RATED\text{-}CAP}$ reduced | $V_{RATED\text{-}CAP}$ | 75 V | 426 | 26.64 | 95.11 |
| | $V_{RATED\text{-}DIODE}$ | 150 V | | | |
| | $r_{SW}$ | 0.1 Ω | | | |
| | $C$ | 4.7 µF | | | |
| | $V_f$ | 1 V | | | |
| 3 $V_{RATED\text{-}DIODE}$ reduced | $V_{RATED\text{-}CAP}$ | 100 V | 944 | 58.57 | 95.12 |
| | $V_{RATED\text{-}DIODE}$ | 150 V | | | |
| | $r_{SW}$ | 0.1 Ω | | | |
| | $C$ | 4.7 µF | | | |
| | $V_f$ | 1 V | | | |
| 4 $C$ increased | $V_{RATED\text{-}CAP}$ | 100 V | 857 | 54.53 | 95.16 |
| | $V_{RATED\text{-}DIODE}$ | 150 V | | | |
| | $r_{SW}$ | 0.1 Ω | | | |
| | $C$ | 10 µF | | | |
| | $V_f$ | 1 V | | | |
| 5 $r_{SW}$ increased | $V_{RATED\text{-}CAP}$ | 100 V | 991 | 108.1 | 91.37 |
| | $V_{RATED\text{-}DIODE}$ | 150 V | | | |
| | $r_{SW}$ | 0.5 Ω | | | |
| | $C$ | 4.7 µF | | | |
| | $V_f$ | 1V | | | |
| 6 $V_f$ increased | $V_{RATED\text{-}CAP}$ | 100 V | 955 | 70.53 | 94.20 |
| | $V_{RATED\text{-}DIODE}$ | 150 V | | | |
| | $r_{SW}$ | 0.1 Ω | | | |
| | $C$ | 4.7 µF | | | |
| | $V_f$ | 2 V | | | |

The results from this section indicate that a better metric is required to complement the mean time to failure. Case 5 suggests that the lossier switches guarantee higher reliability; however, this

is at the cost of degraded efficiency due to higher conduction losses. Thus, a higher *MTTF* comes at the cost of severely degraded performance. Quantifying this degradation would provide a better perspective on the functionality of the converter. We thus utilize the metric of the expected system efficiency (104).

If we assume that the PV system is installed at a tilt angle equal to the latitude -15$^{o}$, over the course of the year, the site receives 5.5 hours per day of one-sun insolation. Equation (20) then yields the capacity factor at the installation,

$$CF = \frac{\left(\frac{h}{day}\right)_{one-sun}}{24\left(\frac{h}{day}\right)} = \frac{5.5}{24} = 22.9\% \tag{133}$$

For the three-phase converter analyzed in this section, the expected energy loss, *EEL*, can be expressed as

$$EEL = CF\left[\frac{P_{LOSS-00}}{\lambda_{00-00}} + \frac{P_{LOSS-01}}{\lambda_{01-01}} + \frac{P_{LOSS-02}}{\lambda_{02-02}} + \frac{P_{LOSS-10}}{\lambda_{10-10}} + \frac{P_{LOSS-11}}{\lambda_{11-11}} + \frac{P_{LOSS-12}}{\lambda_{12-12}} + \frac{P_{LOSS-20}}{\lambda_{20-20}} + \frac{P_{LOSS-21}}{\lambda_{21-21}} + \frac{P_{LOSS-22}}{\lambda_{22-22}}\right] \tag{134}$$

Substituting the failure rates,

$$\begin{aligned} EEL = CF\Bigg[ & \frac{P_{LOSS-00}}{3(\lambda_{CAP00} + \lambda_{SW0} + \lambda_{D0})} + \frac{P_{LOSS-01}}{2\lambda_{CAP01} + 3(\lambda_{SW0} + \lambda_{D0})} + \frac{P_{LOSS-02}}{\lambda_{CAP02} + 3(\lambda_{SW0} + \lambda_{D0})} \\ & + \frac{P_{LOSS-10}}{3\lambda_{CAP10} + 2(\lambda_{SW1} + \lambda_{D1})} + \frac{P_{LOSS-11}}{2(\lambda_{CAP11} + \lambda_{SW1} + \lambda_{D1})} + \frac{P_{LOSS-12}}{\lambda_{CAP12} + 2(\lambda_{SW1} + \lambda_{D1})} \\ & + \frac{P_{LOSS-20}}{3\lambda_{CAP20} + \lambda_{SW2} + \lambda_{D2}} + \frac{P_{LOSS-21}}{2\lambda_{CAP21} + \lambda_{SW2} + \lambda_{D2}} + \frac{P_{LOSS-22}}{\lambda_{CAP22} + \lambda_{SW2} + \lambda_{D2}}\Bigg] \end{aligned} \tag{135}$$

The expected energy produced by the PV module, *EPV*, can be described as

$$EPV = (CF)(P)\left[\frac{1}{3(\lambda_{CAP00}+\lambda_{SW0}+\lambda_{D0})}+\frac{1}{2\lambda_{CAP01}+3(\lambda_{SW0}+\lambda_{D0})}+\frac{1}{\lambda_{CAP02}+3(\lambda_{SW0}+\lambda_{D0})}\right.$$
$$+\frac{1}{3\lambda_{CAP10}+2(\lambda_{SW1}+\lambda_{D1})}+\frac{1}{2(\lambda_{CAP11}+\lambda_{SW1}+\lambda_{D1})}+\frac{1}{\lambda_{CAP12}+2(\lambda_{SW1}+\lambda_{D1})}$$
$$\left.+\frac{1}{3\lambda_{CAP20}+\lambda_{SW2}+\lambda_{D2}}+\frac{1}{2\lambda_{CAP21}+\lambda_{SW2}+\lambda_{D2}}+\frac{1}{\lambda_{CAP22}+\lambda_{SW2}+\lambda_{D2}}\right] \quad (136)$$

The *EEL* and *ESE* are computed for each of the five case studies and the results are tabulated in Table 8. These metrics eliminate the ambiguity noticed with the *MTTF* earlier. As expected, for cases 5 and 6, lossier switches guarantee a higher *MTTF* at the cost of a lower *ESE*.

To conclude the discussion on the three-phase converter, consider the mean sojourn times (described in Section 5.3.2) in possible states. Figure 48 depicts the mean sojourn times for different topological instants that emanate from the three-phase converter for the base case considered in simulation runs before.

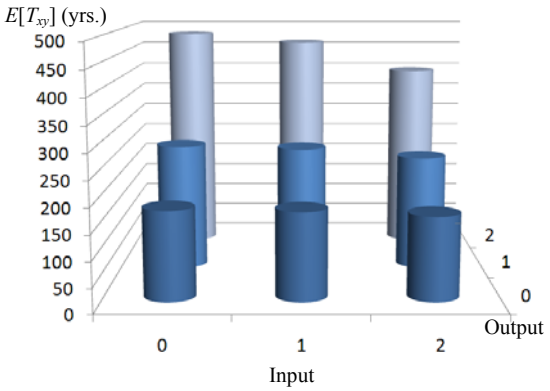


**Figure 48:** Mean sojourn times in different states

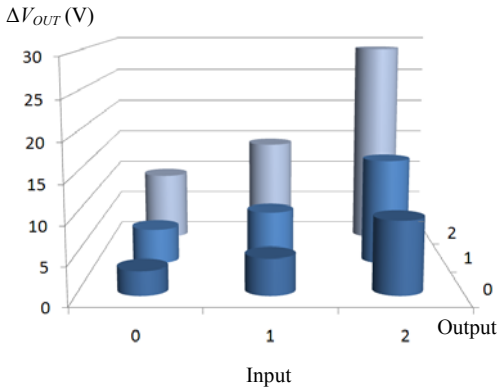


**Figure 49:** Voltage ripple in different states

Figure 48 suggests that as more input stages fail, the mean sojourn time decreases. This is in contrast to failures in output stages, which increase the mean sojourn time. To appreciate this effect, consider the expression for the mean sojourn time of a state *ij* in an *N*-phase converter,

$$E[T_{ij}] = \frac{1}{(N-j)\lambda_{CAPij}+(N-i)(\lambda_{SWij}+\lambda_{Dij})} \quad (137)$$

Since it has been well established that the failure rates of the capacitors dominate over the switches, the above expression can be approximated as

$$E[T_{ij}] \approx \frac{1}{(N-j)\lambda_{CAPij}} \tag{138}$$

For a given number of failed input stages ($i$), as the number of failed output stages ($j$) increases, the product $(N\text{-}j)\lambda_{CAPij}$ is likely to decrease. The increase in voltage ripple caused by the loss of capacitors forces $\lambda_{CAPij}$ to be a monotonically increasing function of $j$, but the factor ($N$-$j$) overshadows this effect. This explains the increase in the mean sojourn time with failures in the output stages. For a given number of failed output stages, $j$, as input stages fail, the most significant parameter that is altered is the output-voltage ripple. This is illustrated in Figure 49, which depicts the output voltage ripple as a function of the number of operational input and output stages. The voltage ripple is noted to be a monotonically increasing function in the number of failed input stages. This explains the decrease in the mean sojourn time with failures in input stages.

### 5.4.2 Two-phase converter

The Kolmogorov forward equations for the two-phase converter (state-transition diagram in Figure 41) can be expressed as:

$$\frac{d\mathbf{P}(t)}{dt} = \mathbf{P}\boldsymbol{\Lambda} \tag{139}$$

where

$$\boldsymbol{\Lambda} = \begin{bmatrix} -2(\lambda_{CAP00}+\lambda_{SW0}+\lambda_{D0}) & 2\lambda_{CAP00} & 2(\lambda_{SW0}+\lambda_{D0}) \\ 0 & -\lambda_{CAP01}-2(\lambda_{SW0}+\lambda_{D0}) & 0 \\ 0 & 0 & -2\lambda_{CAP10}-2(\lambda_{SW1}+\lambda_{D1}) \\ 0 & 0 & 0 \\ 0 & 0 & 0 \end{bmatrix} \begin{matrix} \cdots \\ \cdots \\ \cdots \end{matrix} \begin{bmatrix} 0 & 0 \\ 2(\lambda_{SW0}+\lambda_{D0}) & \lambda_{CAP01} \\ 2\lambda_{CAP10} & 2(\lambda_{SW1}+\lambda_{D1}) \\ -(\lambda_{CAP11}+\lambda_{SW1}+\lambda_{D1}) & (\lambda_{CAP11}+\lambda_{SW1}+\lambda_{D1}) \\ 0 & 0 \end{bmatrix} \tag{140}$$

$$\mathbf{P}(t) = [P_{00}(t) \quad P_{01}(t) \quad P_{10}(t) \quad P_{11}(t) \quad P_{22}(t)] \tag{141}$$

As before, we assume the converter begins operation with all phases completely functional:

$$\mathbf{P}(0) = [1 \quad 0 \quad 0 \quad 0 \quad 0] \tag{142}$$

Consider the following matrix differential equation in the reduced-order state space:

$$\frac{d\mathbf{P_R}(t)}{dt} = \mathbf{P_R}\mathbf{\Lambda_R} \tag{143}$$

where $\mathbf{\Lambda_R}$ is the same as (140) without the last row, and $\mathbf{P_R}(t)$ is defined as

$$\mathbf{P_R}(t) = [P_{00}(t) \quad P_{01}(t) \quad P_{10}(t) \quad P_{11}(t)] \tag{144}$$

The initial-condition vector is modified to

$$\mathbf{P_R}(0) = [1 \quad 0 \quad 0 \quad 0] \tag{145}$$

Taking the Laplace transform of both sides in (143) yields the following linear equations:

$$-2(\lambda_{CAP00} + \lambda_{SW0} + \lambda_{D0})P_{00}^*(s) = sP_{00}^*(s) - 1 \tag{146}$$

$$2\lambda_{CAP00}P_{00}^*(s) + [-\lambda_{CAP01} - 2(\lambda_{SW0} + \lambda_{D0})]P_{01}^*(s) = sP_{01}^*(s) \tag{147}$$

$$2(\lambda_{SW0} + \lambda_{D0})P_{00}^*(s) + [-2\lambda_{CAP10} - (\lambda_{SW1} + \lambda_{D1})]P_{10}^*(s) = sP_{10}^*(s) \tag{148}$$

$$2(\lambda_{SW0} + \lambda_{D0})P_{01}^*(s) + (2\lambda_{CAP10})P_{10}^*(s) + [-\lambda_{CAP11} - \lambda_{SW1} - \lambda_{D1})]P_{11}^*(s) = sP_{11}^*(s) \tag{149}$$

As before, equations (146)-(149) can be solved for the transition probabilities,

$$P_{00}^*(s) = \frac{1}{s + 2(\lambda_{CAP00} + \lambda_{SW0} + \lambda_{D0})} \tag{150}$$

$$P_{01}^*(s) = \frac{2\lambda_{CAP00}}{[s + \lambda_{CAP01} + 2(\lambda_{SW0} + \lambda_{D0})]}P_{00}^*(s) \tag{151}$$

$$P_{10}^{*}(s) = \frac{2(\lambda_{SW0} + \lambda_{D0})}{[s + 2\lambda_{CAP10} + (\lambda_{SW1} + \lambda_{D1})]} P_{00}^{*}(s) \tag{152}$$

$$P_{11}^{*}(s) = \frac{2(\lambda_{SW0} + \lambda_{D0})}{[s + \lambda_{CAP11} + \lambda_{SW1} + \lambda_{D1})]} P_{01}^{*}(s) + \frac{(2\lambda_{CAP10})}{[s + \lambda_{CAP11} + \lambda_{SW1} + \lambda_{D1})]} P_{10}^{*}(s) \tag{153}$$

The *MTTF* of the converter can then be computed from (154)-(155):

$$R^{*}(s) = P_{00}^{*}(s) + P_{01}^{*}(s) + P_{10}^{*}(s) + P_{11}^{*}(s) \tag{154}$$

$$MTTF = R^{*}(0) = P_{00}^{*}(0) + P_{01}^{*}(0) + P_{10}^{*}(0) + P_{11}^{*}(0) \tag{155}$$

As before, the expected energy loss can be estimated as:

$$EEL = CF\left[\frac{P_{LOSS-00}}{\lambda_{00-00}} + \frac{P_{LOSS-01}}{\lambda_{01-01}} + \frac{P_{LOSS-10}}{\lambda_{10-10}} + \frac{P_{LOSS-11}}{\lambda_{11-11}}\right] \tag{156}$$

Substituting for the failure rates,

$$EEL = CF\left[\frac{P_{LOSS-00}}{2(\lambda_{CAP00} + \lambda_{SW0} + \lambda_{D0})} + \frac{P_{LOSS-01}}{\lambda_{CAP01} + 2(\lambda_{SW0} + \lambda_{D0})} + \frac{P_{LOSS-10}}{2\lambda_{CAP10} + \lambda_{SW1} + \lambda_{D1}} + \frac{P_{LOSS-11}}{\lambda_{CAP11} + \lambda_{SW1} + \lambda_{D1}}\right] \tag{157}$$

The expected energy produced by the PV module can be described as

$$EPV = (CF)(P)\left[\frac{1}{2(\lambda_{CAP00} + \lambda_{SW0} + \lambda_{D0})} + \frac{1}{\lambda_{CAP01} + 2(\lambda_{SW0} + \lambda_{D0})} + \frac{1}{2\lambda_{CAP10} + \lambda_{SW1} + \lambda_{D1}} + \frac{1}{\lambda_{CAP11} + \lambda_{SW1} + \lambda_{D1}}\right] \tag{158}$$

The expressions for *EEL* and *EPV* can be substituted in (120) to provide the expected system efficiency. The *MTTF*, *ESE*, and *EEL* are computed for the two-phase converter using the expressions above for the same set of atmospheric constraints as before. The converter specifications are the same as before, but with a reduced number of phases. Effects on

performance due to reduced ratings, lossier switches and higher capacitance are evaluated. The results are documented in Table 9.

TABLE 9
*MTTF*, *EEL*, *ESE* – TWO PHASE CONVERTER

| Case Study | Component Specifications | | MTTF (YEARS) | EEL (MW-s) | ESE (%) |
|---|---|---|---|---|---|
| 1 Base Case | $V_{RATED\text{-}CAP}$ | 110 V | 934 | 32.76 | 95.89 |
| | $V_{RATED\text{-}DIODE}$ | 150 V | | | |
| | $r_{SW}$ | 0.1 Ω | | | |
| | $C$ | 4.7 μF | | | |
| | $V_f$ | 1 V | | | |
| 2 $V_{RATED\text{-}CAP}$ reduced | $V_{RATED\text{-}CAP}$ | 82.5 V | 428 | 15.11 | 95.88 |
| | $V_{RATED\text{-}DIODE}$ | 150 V | | | |
| | $r_{SW}$ | 0.1 Ω | | | |
| | $C$ | 4.7 μF | | | |
| | $V_f$ | 1 V | | | |
| 3 $V_{RATED\text{-}DIODE}$ reduced | $V_{RATED\text{-}CAP}$ | 110 V | 934 | 32.76 | 95.88 |
| | $V_{RATED\text{-}DIODE}$ | 100 V | | | |
| | $r_{SW}$ | 0.1 Ω | | | |
| | $C$ | 4.7 μF | | | |
| | $V_f$ | 1 V | | | |
| 4 $C$ increased | $V_{RATED\text{-}CAP}$ | 110 V | 827 | 29.99 | 95.91 |
| | $V_{RATED\text{-}DIODE}$ | 150 V | | | |
| | $r_{SW}$ | 0.1 Ω | | | |
| | $C$ | 15 μF | | | |
| | $V_f$ | 1 V | | | |
| 5 $r_{SW}$ increased | $V_{RATED\text{-}CAP}$ | 110 V | 977 | 65.04 | 92.13 |
| | $V_{RATED\text{-}DIODE}$ | 150 V | | | |
| | $r_{SW}$ | 0.5 Ω | | | |
| | $C$ | 4.7 μF | | | |
| | $V_f$ | 1V | | | |
| 6 $V_f$ increased | $V_{RATED\text{-}CAP}$ | 110 V | 946 | 40.61 | 94.96 |
| | $V_{RATED\text{-}DIODE}$ | 150 V | | | |
| | $r_{SW}$ | 0.1 Ω | | | |
| | $C$ | 4.7 μF | | | |
| | $V_f$ | 2 V | | | |

Similar trends as the three-phase converter are noticed. Higher capacitance and lower capacitor voltage rating severely reduce the *MTTF*. The diode voltage rating is not as significant. In addition, lossier switches provide a higher *MTTF* at the expense of reduced *ESE*.

### 5.4.3 *N*-phase converter

To assess the reliability of an *N*-phase converter, define a Markov process $\{X(t), t \geq 0\}$ over the state space, $S$=$\{00, 01, 02, \ldots.NN\}$. To generalize the discussion, consider the following description of states in $S$:

a. State 00: Converter operational
b. State $ij$: $i$ input and $j$ output phases failed. $(0 \leq i \leq N-1, 0 \leq j \leq N-1)$
c. State $NN$: Converter failed

It is evident that this topology has $N^2$ operational states and one failed state. The reduced-order transition probability vector is of the form

$$\mathbf{P_R}(t) = [P_{00}(t) \quad P_{01}(t) \quad P_{02}(t) \quad .. \quad P_{ij}(t) \quad .. \quad P_{(N-1)(N-1)}(t)] \tag{159}$$

The element that has been eliminated from the full-order model is the probability of existence in the failed state, $P_{NN}(t)$. As before, the initial conditions required are

$$\mathbf{P_R}(0) = [1 \quad 0 \quad 0 \quad .. \quad 0 \quad .. \quad 0] \tag{160}$$

Based on the analysis of the three-phase and two-phase converter, useful inferences can be drawn which aid in the derivation of the Laplace transform of the transition probabilities.

- Except for the failed state, every state has at most two transitions leading to it.
- States of the form 0$i$ and $i$0, $i > 0$, have just one transition leading to them.
- All other non-failed states have two transitions leading into them.
- The fully operational state, 00, has no transitions leading into it.
- With reference to the state-transition diagrams presented earlier, the failure rates corresponding to a transition from state $ij$ to state $i(j+1)$ represent the failure of an output stage (capacitor). The failure rate accompanying such a transition is of the form $(N_c-j)\lambda_{CAPij}$. Since we emphasize designs where the number of output phases and input phases are the same initially, the above failure rate can be expressed as $(N-j)\lambda_{CAPij}$.
- Similarly, the failure rates corresponding to a transition from state $ij$ to state $(i+1)j$ represent failure of an input stage (active switch or diode). The failure rate accompanying such a transition is of the form $(N-i)$ $(\lambda_{SWi} + \lambda_{Di})$.
- Transitions from states of the general form $(N-1)j$ to state $NN$ are at the rate $(\lambda_{SWi} + \lambda_{Di})$. Similarly, transitions from states of the general form $i(N-1)$ to state $NN$ are at the rate $\lambda_{CAPi(N-1)}$

These transitions and associated failure rates are illustrated in Figure 50, which depicts relevant sections of the state-transition diagram of an $N$-phase converter.

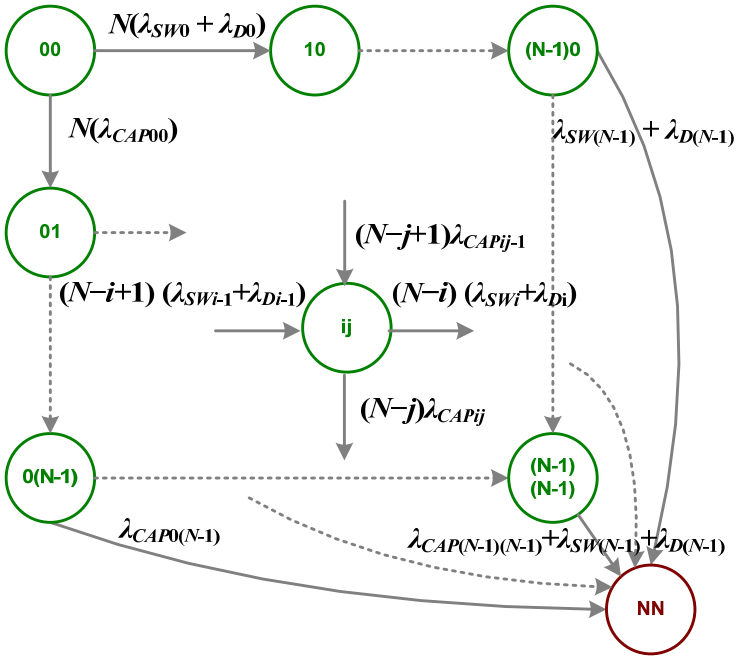


**Figure 50:** Relevant sections of state-transition diagram for *N*-phase converter

Based on these inferences, we can express the Laplace transform of a given transition probability, $P_{ij}^{*}(s)$, as

$$P_{ij}^{*}(s)=\frac{(N-j+1)(\lambda_{CAPi(j-1)})}{[s+(N_c-j)\lambda_{CAPij}+(N-i)(\lambda_{SWi}+\lambda_{Di})]}P_{i(j-1)}^{*}(s)+\frac{(N-i+1)(\lambda_{SW(i-1)}+\lambda_{D(i-1)})}{[s+(N_c-j)\lambda_{CAPij}+(N-i)(\lambda_{SWi}+\lambda_{Di})]}P_{(i-1)j}^{*}(s) \tag{161}$$

In the above expressions if any of the indices are less than zero, the term is disregarded. Finally, the Laplace transform of the initial state, $P_{00}^{*}(s)$, is expressed as

$$P_{00}^{*}(s)=\frac{1}{[s+(N_c)\lambda_{CAP00}+(N)(\lambda_{SW0}+\lambda_{D0})]} \tag{162}$$

For simplification, enforcing an equal number of input and output phases simplifies the above expressions to:

$$P_{ij}^{*}(s)=\frac{(N-j-1)(\lambda_{CAPi(j-1)})}{[s+(N-j)\lambda_{CAPij}+(N-i)(\lambda_{SWi}+\lambda_{Di})]}P_{i(j-1)}^{*}(s)$$
$$+\frac{(N-i-1)(\lambda_{SW(i-1)}+\lambda_{D(i-1)})}{[s+(N-j)\lambda_{CAPij}+(N-i)(\lambda_{SWi}+\lambda_{Di})]}P_{(i-1)j}^{*}(s) \quad (163)$$

$$P_{00}^{*}(s)=\frac{1}{[s+N(\lambda_{CAP00}+\lambda_{SW0}+\lambda_{D0})]} \quad (164)$$

Given these general expressions, the *MTTF* can be computed as:

$$MTTF=\sum_{i=0}^{N-1}\sum_{j=0}^{N-1}P_{ij}^{*}(0) \quad (165)$$

## 5.5 Trends and Comparisons

The variation of the *MTTF* and *ESE* as a function of dominant design parameters such as the voltage rating of the capacitor, $V_{RATING\_CAP}$, value of capacitance, $C$, switch resistance, $r_{SW}$, and switching frequency, $f$, is assessed. In each of the plots described below, apart from the independent quantity, all other circuit parameters are assumed to be the same as the base cases (Tables 8, 9).

Figures 51-52 depict the variation of the *MTTF* and *ESE* (respectively) of the three- and two-phase converters with switch resistance, $r_{SW}$, varied.

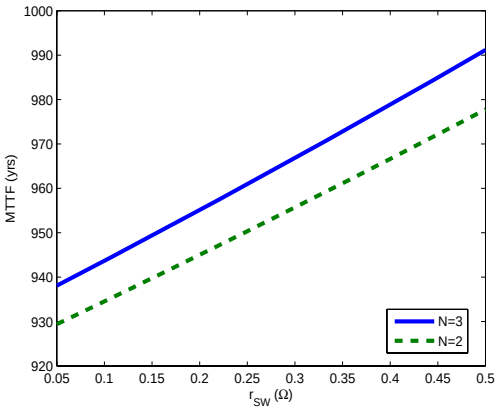


**Figure 51:** *MTTF* as a function of switch resistance

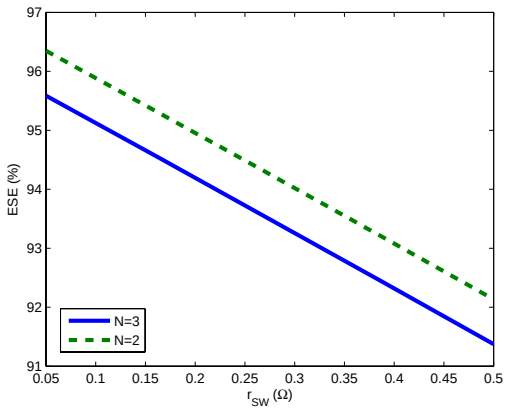


**Figure 52:** *ESE* as a function of switch resistance

For the range of switch resistance considered, the three-phase converter has a higher *MTTF* than its two-phase counterpart at the cost of lower expected system efficiency.

Figure 53 depicts the variation of the MTTF with the rating of the output capacitors, $V_{RATING\text{-}CAP}$. Comparing Figure 53 with Figure 51 evinces that the *MTTF* is more sensitive to the voltage rating of the output capacitors as compared to the switch resistance. Additionally, over all voltage ratings, we can guarantee a higher *MTTF* with the three-phase converter than with the two-phase converter.

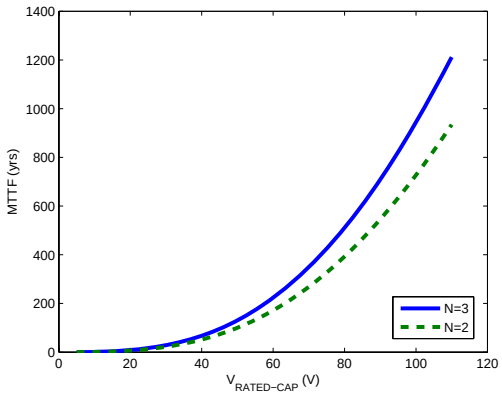


**Figure 53:** *MTTF* as a function of capacitor voltage rating

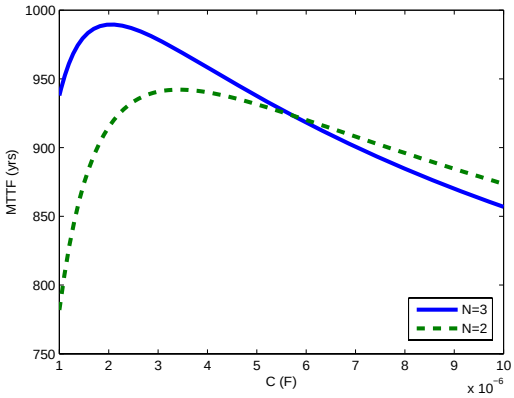


**Figure 54:** *MTTF* as a function of capacitance value

Figure 54 investigates the impact of the choice of capacitance on the *MTTF* of two- and three-phase converters. For a fair comparison, in this case study and the next, the capacitors in the two-phase converter are rated for 110 V while those in the three-phase converter are rated for 100 V. This ensures a fair comparison in that, for the base case specifications attached in Table 4, the *MTTF* of the two converters is almost the same. The results illustrate that for each converter, there is an optimal capacitance value that maximizes the *MTTF*. Also, note that topological redundancy does not necessarily guarantee improved reliability. For capacitances below 6 μF, the voltage stress tends to dominate and a higher number of phases guarantee improved reliability. Beyond 6 μF, the degradation in the failure rate due to high capacitance and the higher voltage rating of the capacitors in the two-phase converter overshadow the voltage stress factor, making the two-phase converter more reliable.

Finally, we consider the impact of switching frequency on the *MTTF*. The predominant effect is the reduction in output voltage ripple with higher switching frequencies. This reduces the voltage stress on the output capacitors, hence extending their expected lifetime. Figure 55

indicates that this effect is only valid up to 12 kHz. Beyond that, the higher voltage rating of the capacitors in the two-phase converter causes this topology to be more reliable across all possible switching frequencies.

For cases that do not directly influence the power loss in the converter, the *ESE* is not very instructive of performance. For instance, we depict in Figure 56, the *ESE* of the two- and three-phase converters as a function of the switching frequency. The difference in the curves is a function of the probabilistic nature of the definition of the *ESE* and not indicative of degraded performance (no frequency-dependent loss models were utilized).

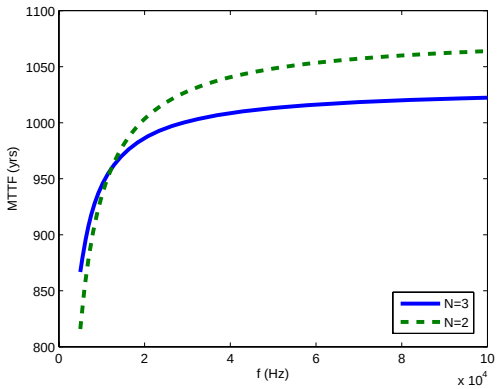


**Figure 55:** *MTTF* as a function of switching frequency

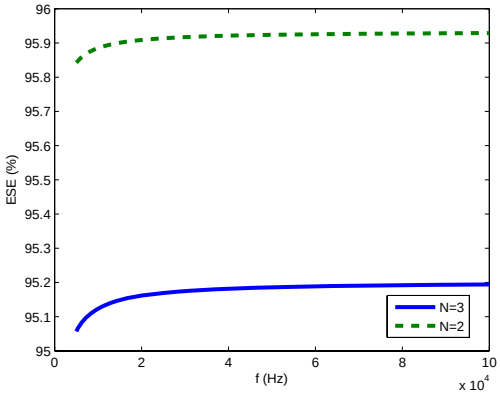


**Figure 56:** *ESE* as a function of switching frequency

# CHAPTER 6

## CONCLUSIONS AND FUTURE WORK

A comprehensive design procedure that integrates performance and reliability metrics is suggested for topologically redundant switch-mode power converters in PV-energy conversion applications. The analysis begins with a detailed description of the steady-state operation of a candidate multiphase boost converter topology. The analytical description of the converter provides expressions to rapidly quantify the operational stresses on the components. Next, the variation of the failure-rates of the devices is analyzed across a wide range of representative ambient conditions and converter design choices. Finally, a Markov reliability model is derived for a generic *N*-phase converter that enables the evaluation of system-reliability metrics such as the mean time to failure. The progression of the design strategy is illustrated in Figure 57. Highlighted in Figure 58 is a possible design strategy for the converter analyzed in this work. Notice the overlap in design tasks which would be otherwise construed as entirely linked to reliability assessment or performance evaluation.

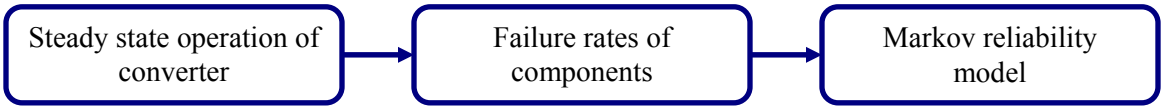


**Figure 57:** Analysis flow

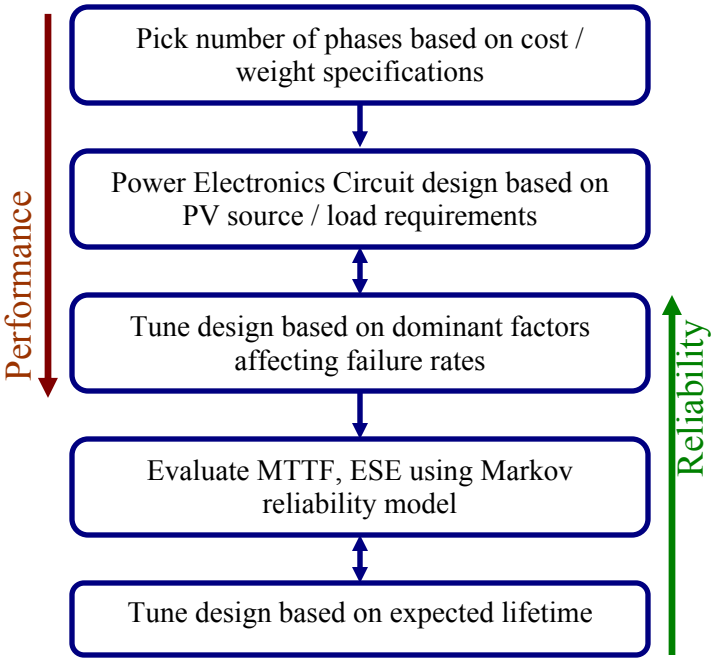


**Figure 58:** Possible design strategy

Future research may investigate the application of time-varying failure rates to the analysis. In addition, numerical optimization tools could suggest optimal converter specifications, given bounds on performance, reliability, weight or cost. Asymmetric designs in which the number of output capacitors is not the same as the number of input phases could be investigated. More accurate thermal models could be used to specify the device failure rates. Finally, similar tools could be employed to specify the reliability of other power-electronic converters such as inverters and rectifiers.

# APPENDIX

## MATLAB CODE FOR THREE-PHASE CONVERTER

This appendix contains code, written in the MATLAB language, to compute the *MTTF* of a representative three-phase converter.

```
%%%%%%%%%%%% %MTTF COMPUTATION 3-PHASE CONVERTER%%%%%%%%
% Preliminaries
clc; clear all;

% Ambient conditions, PV module and converter description
S=1000; T=85;
Isc=5.99; Voc=48.7; Im=5.61; Vm=41;
dT=T-25;dS=(S/1000)-1;
Iscp=Isc*(S/1000)+0.0035*dT; Imp=Im*(S/1000)+0.0035*dT;
Vocp=Voc-0.001325*dT; Vmp=Vm-0.001325*dT;
I=Imp; N=3; Nc=3; R=50; Vf=1; rsw=0.1; rl=0.1; f=10e3;Vin=Vmp;
L=120e-5; M=118e-5; Leff=(L^2+(N-2)*M*L-(N-1)*M^2)/(L-M);

%% Capacitor Failure Rates
Vrated_cap=100; C=4.7e-6; lcap=zeros(N,Nc);
%lcap00 lcap01 lcap02
%lcap10 lcap11 lcap12
%lcap20 lcap21 lcap22
% i-1 represents number of failed input phases
% j-1 represents number of failed output phases
env_cap=2; quality_cap=10;
for i=1:N
   for j=1:Nc
      c1(i,j)=I^2*R*(N-i+1)^2;
      c2(i,j)=(N-i+1)*I^2*rsw-I*Vf*(N-i+1)-2*(N-i+1)*I^2*R;
      c3(i,j)=I^2*R-Vin*I+I^2*rl+I*Vf;
      Df(i,j)=min((roots([c1(i,j) c2(i,j) c3(i,j)])));
      Dd(i,j)=(1/(N-i+1))-Df(i,j);
      Vout(i,j)=I.*R.*(1-Df(i,j)*(N-i+1));
      dvoutdt(i,j)=((I-Vout(i,j)/R)*(Dd(i,j)))/(f*(Nc-j+1)*C);
      Scap(i,j)=(Vout(i,j)+(dvoutdt(i,j)/2))/(Vrated_cap);
```

```
      base_cap(i,j)=0.0028*((Scap(i,j)/0.55)^3+1)*exp(4.09*((T+273)/(358)^5.9));
      cv=0.32*(C/(10^-6))^0.19;
      lcap(i,j)=base_cap(i,j)*cv*env_cap*quality_cap;
   end
end

%% Switch Failure rates
% Diode
Vrated_diode=150; env_diode=0.6; quality_diode=8; base_diode=0.003;
ldiode=zeros(1,N);
%ldiode=[ld0 ld1 ld2]

%Switch
Prated=200; application_fet=8; base_fet=0.012; env_fet=0.6; quality_fet=8;
lsw=zeros(1,N);
%lsw=[lsw0 lsw1 lsw2]

% Inductor Loss: N I^2 rL
% Switch Loss: N I^2 rsw Dsw
% Diode drop: N I Vf Dd

for i=1:N
   % Diode
   c1(i)=I^2*R*(N-i+1)^2;
   c2(i)=(N-i+1)*I^2*rsw-I*Vf*(N-i+1)-2*(N-i+1)*I^2*R;
   c3(i)=I^2*R-Vin*I+I^2*rl+I*Vf;
   Df(i)=min((roots([c1(i) c2(i) c3(i)])));
   Dd(i)=(1/(N-i+1))-Df(i);
   Vout(i)=I*R*(1-Df(i)*(N-i+1));
   if(Vout(i)/Vrated_diode)<=0.3
      Sdiode(i)=0.054;
   else
      Sdiode(i)=(Vout(i)/Vrated_diode)^2.43;
   end
   Tc_diode(i)=T+30;
   theta_diode=5;
   Ploss_diode(i)=Vf*I*Dd(i);
```

```
    Tj_diode(i)=Tc_diode(i)+Ploss_diode(i)*theta_diode;
    temp_diode(i)=exp(-3091*((Tj_diode(i)+273)^-1)-((298)^-1));
    ldiode(i)=base_diode*temp_diode(i)*Sdiode(i)*env_diode*quality_diode;

    %Switch
    Tc_fet(i)=T+30;
    theta_fet=5;
    Ploss_fet(i)=I*I*rsw*Df(i);
    Tj_fet(i)=Tc_fet(i)+Ploss_fet(i)*theta_fet;
    temp_fet(i)=exp(-1925.*((Tj_fet(i)+273).^-1)-((298)^-1));
    lsw(i)=base_fet*temp_fet(i)*application_fet*env_fet*quality_fet;
    Pind(i)=(N-i+1)*(I^2)*rl;
    Psw(i)=(N-i+1)*(I^2)*rsw*Df(i);
    Pd(i)=(N-i+1)*(I*Vf*Dd(i));
end

%% MTTF COMPUTATION
lcap00=lcap(1,1);lcap01=lcap(1,2);lcap02=lcap(1,3);
lcap10=lcap(2,1);lcap11=lcap(2,2);lcap12=lcap(2,3);
lcap20=lcap(3,1);lcap21=lcap(3,2);lcap22=lcap(3,3);
lsw0=lsw(1);lsw1=lsw(2);lsw2=lsw(3);
ld0=ldiode(1);ld1=ldiode(2);ld2=ldiode(3);
%% Laplace transform of transition probability
P00=1/(3*(lcap00+lsw0+ld0));
P01=P00*(3*lcap00)/(2*lcap01+3*(lsw0+ld0));
P02=P01*(2*lcap01)/(lcap02+3*(lsw0+ld0));
P10=P00*(3*(lsw0+ld0))/(3*lcap10+2*(lsw1+ld1));
P11=(P01*(3*(lsw0+ld0))/(2*lcap11+2*(lsw1+ld1)))+(P10*(3*lcap10)/(2*lcap11+2*(lsw1+ld1)));
P12=(P02*(3*(lsw0+ld0))/(lcap12+2*(lsw1+ld1)))+(P11*(2*lcap11)/(lcap12+2*(lsw1+ld1)));
P20=P10*(2*(lsw1+ld1))/(3*lcap20+lsw2+ld2);
P21=(P11*(2*(lsw1+ld1))/(2*lcap21+lsw2+ld2))+(P20*(3*lcap20)/(2*lcap21+lsw2+ld2));
P22=(P12*(2*(lsw1+ld1))/(lsw2+ld2+lcap22))+(P21*(2*lcap21)/(lcap22+lsw2+ld2));
MTTF=P00+P01+P02+P10+P11+P12+P20+P21+P22;
MTTFyears=(MTTF*10^6)/(8760); MTTFhours=MTTF*8760;

%% EEL Computation
CF=5.5/24;
```

```
power00=Pind(1)+Psw(1)+Pd(1);
power01=power00;
power02=power00;
power10=Pind(2)+Psw(2)+Pd(2);
power11=power10;
power12=power10;
power20=Pind(3)+Psw(3)+Pd(3);
power21=power20;
power22=power20;

eel=CF*((power00/(3*(lcap00+lsw0+ld0)))+(power01/(2*lcap01+3*(lsw0+ld0)))+(power02/(lcap02+3*(ls
w0+ld0)))+(power10/(3*lcap10+2*(lsw1+ld1)))+(power11/(2*lcap11+2*(lsw1+ld1)))+(power12/(lcap12+
2*(lsw1+ld1)))+(power20/(3*lcap20+lsw2+ld2))+(power21/(2*lcap21+lsw2+ld2))+(power22/(lcap22+lsw
2+ld2)));
eel=(eel*10^6);
eelMWHr=eel/(10^6);

eprod=CF*10^6*230*((1/(3*(lcap00+lsw0+ld0)))+(1/(2*lcap01+3*(lsw0+ld0)))+(1/(lcap02+3*(lsw0+ld0)
))+(1/(3*lcap10+2*(lsw1+ld1)))+(1/(2*lcap11+2*(lsw1+ld1)))+(1/(lcap12+2*(lsw1+ld1)))+(1/(3*lcap20+l
sw2+ld2))+(1/(2*lcap21+lsw2+ld2))+(1/(lcap22+lsw2+ld2)));
ESE=100*(1-eel/eprod);
```

## REFERENCES


[1] P. Wong, P. Xu, B. Yang, and F. C. Lee, "Performance improvements of interleaving VRMs with coupling inductors," *IEEE Trans. Power Electronics*, vol. 16, pp. 499-507, July 2001.

[2] B. A. Miwa, D. M. Otten, and M. F. Schlecht, "High efficiency power factor correction using interleaving techniques," in *Proc. IEEE Applied Power Electronics Conference and Exhibition*, 1992, pp. 557-568.

[3] S. Dwari and L. Parsa, "A novel high efficiency high power interleaved coupled-inductor boost Dc-Dc converter for hybrid and fuel cell electric vehicle," in *Proc. Vehicle Power and Propulsion Conference*, 2007, pp. 309-404.

[4] C. Chang and M. A. Knights, "Interleaving technique in distributed power conversion systems," *IEEE Trans. Circuits and Systems-I: Fundamental Theory and Applications*, vol. 42, pp. 245-251, May 1995.

[5] F. Liccardo, P. Marino, G. Torre, and M. Triggianese, "Interleaved Dc-Dc converters for photovoltaic modules," in *Proc. International Conference on Clean Electrical Power*, 2007, pp. 201-207.

[6] M. Vázquez, J. M. A. Márquez, and F. S. Manzano, "A methodology for optimizing stand-alone PV-system size using parallel-connected Dc/Dc converters," *IEEE Trans. Industrial Electronics*, vol. 55, pp. 2664-2673, July 2008.

[7] S. Daher, J. Schmid, and F. L. M. Antunes, "Multilevel inverter topologies for stand-alone PV systems," *IEEE Trans. Industrial Electronics*, vol. 55, pp. 2703-2712, July 2008.

[8] J.-P. Lee, B.-D. Min, T.-J. Kim, D.-W. Yoo, and J.-Y. Yoo, "A novel topology for photovoltaic Dc/Dc full-bridge converter with flat efficiency under wide PV module voltage and load range," *IEEE Trans. Industrial Electronics*, vol. 55, pp. 2655-2673, July 2008.

[9] D. J. Perreault and J. G. Kassakian, "Distributed interleaving of paralleled power converters," *IEEE Trans. Circuits and Systems-I: Fundamental Theory and Applications*, vol. 44, pp. 728-734, Aug. 1997.

[10] R. W. Erickson and D. Maksimovic, "A multiple-winding magnetics model having directly measurable parameters," in *Proc. Power Electronics Specialist Conference*, 1998, pp. 1472-1478.

[11] P. Zumel, O. García, J. A. Cobos, and J. Uceda, "Magnetic integration for interleaved converters," in *Proc. IEEE Applied Power Electronics Conference and Exhibition*, 2003, pp. 1143-1149.

[12] M. Veerachary, T. Senjyu, and K. Uezato, "Maximum power point tracking of coupled inductor interleaved boost converter supplied PV system," *IEE Proc.-Electric Power Applications*, vol. 150, pp. 71-80, Jan. 2003.

[13] C. Cabal, A. Cid-Pastor, L. Seguier, B. Estibals, and C. Alonso, "Improved photovoltaic conversion chain with interleaved method," in *Proc. Power Electronics Specialist Conference*, 2008, pp. 70-75.

[14] R. Leyva, C. Alonso, I. Queinnec, A. Cid-Pastor, D. Lagrange, and L. Martinez-Salamero, "MPPT of photovoltaic applications using extremum-seeking control," *IEEE Trans. on Aerospace and Electronic Systems*, vol. 42, pp. 249-258, Jan. 2006.

[15] H.-B. Shin, J.-G. Park, S.-K. Chung, H.-W. Lee, and T. A. Lipo, "Generalized steady-state analysis of multiphase interleaved boost converter with coupled inductors," *IEE Proc.-Electric Power Applications*, vol. 152, pp. 584-594, May 2005.

[16] H.-B. Shin, E.-S. Jang, J.-G. Park, H.-W. Lee, and T. A. Lipo, "Small-signal analysis of multiphase interleaved boost converter with coupled inductors," *IEE Proc.-Electric Power Applications*, vol. 152, pp. 1161-1170, Sep. 2005.

[17] P.-W. Lee, Y.-S. Lee, D. K. W. Cheng, and X.-C. Liu, "Steady-state analysis of an interleaved boost converter with coupled inductors," *IEEE Trans. Industrial Electronics*, vol. 47, pp. 787-795, Aug. 2000.

[18] E. L. Meyer and E. E. van Dyk, "Assessing the reliability and degradation of photovoltaic module performance parameters," *IEEE Trans. on Reliability*, vol. 53, pp. 83-92, Mar. 2004.

[19] M. Vazquez and I. R.-Stolle, "PV module reliability model based on field-degradation studies," *Prog. in Photovoltaics: Research and Appl.*, vol. 16, pp. 419-433, 2008.

[20] N. G. Dhere, "Reliability of PV modules and balance-of-system components," in *Proc. IEEE Photovoltaics Specialists Conf.*, 2005, pp. 1570-1576.

[21] A. Ristow, M. Begovic, A. Pregelj, and A. Rohatgi, "Development of a methodology for improving photovoltaic inverter reliability," *IEEE Trans. Industrial Electronics*, vol. 55, pp. 2581-2592, July 2008.

[22] Y. C. Qin, N. Mohan, R. West, and R. Bonn, "Status and needs of power electronics for photovoltaic inverters," Sandia National Labs., June 2002. [Online]. Available: http://www.prod.sandia.gov/cgi-bin/techlib/access-control.pl/2002/021535.pdf

[23] H. Calleja, F. Chan, and I. Uribe, "Reliability-oriented assessment of a Dc/Dc converter for photovoltaic applications," in *Proc. IEEE Power Electronics Specialist Conference*, 2007, pp. 1522-1527.

[24] F. Chan, H. Calleja, and E. Martinez, "Grid connected PV systems: A reliability-based comparison," in *Proc. IEEE International Symposium on Industrial Electronics*, 2006, pp. 1583-1588.

[25] F. Chan and H. Calleja, "Reliability: A new approach in design of inverters for PV systems," in *Proc. IEEE International Power Electronics Congress*, 2006, pp. 1-6.

[26] G. Petrone, G. Spagnuolo, R. Teodorescu, M. Veerachary, and M. Vitelli, "Reliability issues in photovoltaic power processing systems," *IEEE Trans. on Industrial Electronics*, vol. 55, pp. 2569-2580, July 2008.

[27] A. Dominguez-Garcia and P. T. Krein, "Integrating reliability into the design of fault-tolerant power electronics systems," in *Proc. Power Electronics Specialist Conference*, 2008, pp. 2665-2671.

[28] J. A. Gow and C. D. Manning, "Development of a photovoltaic array model for use in power-electronics simulation studies," *IEE Proc.-Electric Power Applications*, vol. 146, pp. 193-200, Mar. 1999.

[29] M. S. Suresh, "Measurement of solar cell parameters using impedance spectroscopy," *Solar Energy Materials and Solar Cells*, vol. 43, pp. 21-28, Aug. 1996.

[30] D. S. H. Chan, J. R. Phillips, and J. C. H. Phang, "A comparative study of extraction methods for solar cell model parameters," *Solid-State Electronics*, vol. 29, pp. 329-337, Mar. 1986.

[31] S. Jianhui, Y. Shijie, and Z. Wei, "Investigation on engineering analytical model of silicon solar cell," *Acta Energiae Solaris Sinica*, pp. 409-412, 2001.

[32] Sunpower, "SPR-230-WHT, Sunpower 230 Watt PV Module data sheet," Mar. 2009. [Online]. Available: http:// www.sunpowercorp.com.

[33] R. Balog, P. T. Krein, and D. C. Hamill, "Coupled inductors-A basic filter building block," in *Proc. Electrical Manufacturing Coil Winding Association*, 2000, pp. 271-278.

[34] F. Farahmand, F. P. Dawson, and J. D. Lavers, "An assessment of coupled inductor modeling for a multiple output flyback converter," in *Proc. Computers in Power Electronics*, 2006, pp. 310-316.

[35] R. W. Erickson and D. Maksimovic, *Fundamentals of Power Electronics*. New York, NY: Springer Science, 2001.

[36] D. Sera, R. Teodorescu, J. Hantschel, and M. Knoll, "Optimized maximum power point tracker for fast-changing environmental conditions," *IEEE Trans. Industrial Electronics*, vol. 55, pp. 2629-2637, July 2008.

[37] R. Gules, J. Pacheco, H. L. Hey, and J. Imhoff, "A maximum power point tracking system with parallel connection for PV stand-alone applications," *IEEE Trans. Industrial Electronics*, vol. 55, pp. 2674-2683, July 2008.

[38] M. Fortunato, A. Giustiniani, G. Petrone, G. Spagnuolo, and M. Vitelli, "Maximum power point tracking in a one-cycle-controlled single-stage photovoltaic inverter," *IEEE Trans. Industrial Electronics*, vol. 55, pp. 2684-2693, July 2008.

[39] N. Femia, G. Lisi, G. Petrone, G. Spagnuolo and M. Vitelli, "Distributed maximum power point tracking of photovoltaic arrays: Novel approach and system analysis," *IEEE Trans. Industrial Electronics*, vol. 55, pp. 2610-2621, July 2008.

[40] T. Esram and P. L. Chapman, "Comparison of photovoltaic array maximum power point tracking techniques," *IEEE Trans. Energy Conversion*, vol. 22, pp. 439-449, June 2007.

[41] P. T. Krein, "Ripple correlation control, with some applications," in *Proc. IEEE Int. Symposium on Circuits and Systems*, 1999, pp. 283-286.

[42] D. L. Logue and P. T. Krein, "Observer-based techniques in ripple correlation control applied to power electronic systems," in *Proc. IEEE Power Electronics Specialists Conference*, 1999, pp. 2014-2018.

[43] D. L. Logue and P. T. Krein, "Optimization of power electronic systems using ripple correlation control: A dynamic programming approach," in *Proc. IEEE Power Electronics Specialists Conference*, 2001, pp. 459-464.

[44] T. Esram, J. W. Kimball, P. T. Krein, P. L. Chapman, and P. Midya, "Dynamic maximum power point tracking of photovoltaic arrays using ripple correlation control," *IEEE Trans. Power Electronics*, vol. 21, pp. 1282-1291, Sep. 2006.

[45] P. Midya, P. T. Krein, R. J. Turnbull, R. Reppa, and J. Kimball, "Dynamic maximum power point tracker for photovoltaic applications," in *Proc. IEEE Power Electronics Specialists Conference*, 1996, pp. 1710-1716.

[46] Gilbert M. Masters, *Renewable and Efficient Electric Power Systems*. Hoboken, NJ: Wiley-Inter Science, 2004.

[47] Department of Defense, "Reliability prediction of electronic equipment," MIL-HDBK-217F, Jan. 1990.